

7657

7657
JNCASR
621.437 P11

ज.ने.उ.वै.अ.के / JNCASR
Acc. 7657
No.
पुस्तकालय / LIBRARY

Vortex shedding patterns, their competition, and chaos in flow past inline oscillating rectangular cylinders

A Thesis
Submitted for the Degree of
MASTER OF SCIENCE (ENGINEERING)

by
SRIKANTH T



ENGINEERING MECHANICS UNIT
JAWAHARLAL NEHRU CENTRE FOR ADVANCED SCIENTIFIC RESEARCH
(A Deemed University)
Bangalore – 560 064

JULY 2011

621.437

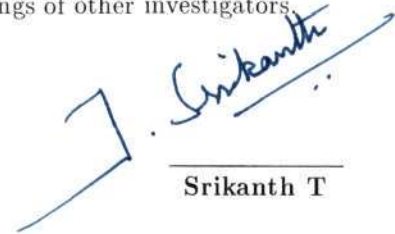
911

To My Family & Lev Landau

DECLARATION

I hereby declare that the matter embodied in the thesis entitled "**Vortex Shedding Patterns, Their Competition, And Chaos In Flow Past Inline oscillating Rectangular Cylinders**" is the result of investigations carried out by me at the Engineering Mechanics Unit, Jawaharlal Nehru Centre for Advanced Scientific Research, Bangalore, India under the supervision of **Prof. Rama Govindarajan** and that it has not been submitted elsewhere for the award of any degree or diploma.

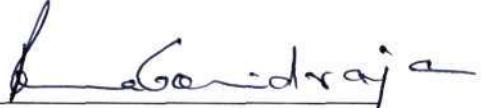
In keeping with the general practice in reporting scientific observations, due acknowledgment has been made whenever the work described is based on the findings of other investigators.



Srikanth T

CERTIFICATE

I hereby certify that the matter embodied in this thesis entitled "**Vortex Shedding Patterns, Their Competition, And Chaos In Flow Past Inline oscillating Rectangular Cylinders**" has been carried out by **Mr. Srikanth T** at the Engineering Mechanics Unit, Jawaharlal Nehru Centre for Advanced Scientific Research, Bangalore, India under my supervision and that it has not been submitted elsewhere for the award of any degree or diploma.


Prof. Rama Govindarajan/
(Research Supervisor)

Acknowledgements

Firstly, I would like to express my gratitude to my *Family* for all the freedom, help, support and encouragement I have received from them. This work would not have been possible without their support.

I would like to express my gratitude to *Prof. Rama Govindarajan* for saving me from *Maruti-Suzuki* and for making me a part of her research group. She has been a teacher and a mentor to me. The freedom she gave me to do things at my own pace has helped me read things unrelated to my work. Her constant support, help and infinite patience have led to the final form of this thesis.

I would like to thank *Prof. K R Sreenivas, Dr. Ganesh Subramanian* and *Dr. Santosh Ansumali* for offering the Heat Transfer, MHD and Basic Fluid Mechanics courses during my first year. I have benefitted a lot from these courses. The lectures on Kinetic Theory by *Dr. Ganesh Subramanian* have piqued my interest in the subject, and I would like to specifically thank him for that.

I would like to thank *Prof. Ram Ramaswamy* for the discussions on chaos and routes to it.

I would like to thank *Harish* for all the help I have received from him right from my undergraduate days at *JNC*. I would like to specifically mention his help with my codes and the pains he endured during debugging them. I also thank him for the collaboration on the vortex shedding problem and for helping me learn the fundamentals of Nonlinear Dynamics.

I have learnt many things through discussions with *Anubhab*. The (hyper-)regular dinner outings, constantly pestering a few people, and Chandraiah coffee 'breaks' with him have been an integral part of my life here. His help with my PhD applications played a crucial role in getting me a place in *Yale*. I shall always be thankful for that.

I thank *Ponnu* for her constant help and company. Discussions on different topics with her have been helpful.

I thank *Sumesh* for all the discussions related to Boltzmann Kinetic Theory, for help with Xmgrace, Matlab and Latex and for proofreading chapter 2 of this thesis. His credit card has been of tremendous help, and life would have been quite difficult without it.

I thank *Ratul* for all the vivid and lively stories and for his company.

Many many thanks to *Dr. Vishwanath Shastry* for his company, discussions and nonstop entertainment- even from the other end of the globe.

I thank *Dabade* for his help with various things and for his lively company.

I thank *Comrade Saikishan* for keeping me on my toes during coursework, for the pizza outings and for the constant enlightenment on *Saurav Ganguly*.

I thank *Vinay* for his help with Latex .

I thank *Croor Singh* for his emails, for his company and for all the debates and discussions we have had.

Prashanth for all the profound PJs and for the discussions.

Many thanks to *Rohith* for generating data for the vortex-merger plots and for the discussions.

I would like to thank *Vivek, Rakshith, Rahul, Gayathri, Krithika, Sharath, Shiwani, Sourabh, Navneeth, Jose, Rajesh, Mamta, Vybhav, Vikram, Divya, Sunil* and others for their help and company.

Anurag, Deepti, Dennis, Jamal, Mayukh, Sandhyaa, Sandy Paul, Sanjeev and *Vijay* have been great friends of mine. I want to thank them for their support and friendship.

Lastly, I would like to thank the *Cambridge University Press* for permitting me to reproduce the figures in Chapter 1.

Abstract

In this thesis, vortex shedding from fixed and inline oscillating rectangular cylinders is investigated for the first time to our knowledge. This is a numerical study, and the Lattice Boltzmann method has been used for simulations. Grid stretching was employed to reduce computation time. Cylinders of different aspect ratios, defined here as the ratio of height to width, namely: 1, 2, 4, 6 and 8 have been used in this study. Critical Reynolds numbers (Re_{cr}) for fixed rectangular cylinders in uniform flow have been calculated, and it is shown that Re_{cr} decreases slightly with increasing D/h . It is also shown that the growth rates of disturbance in the wake varies linearly with $(Re - Re_{cr})$ for rectangular geometries too when Re is close to Re_{cr} as predicted by Landau (Landau & Lifshitz 2005a) and later confirmed by the experiments of Sreenivasan *et al.* (1987) and Provansal *et al.* (1989) on a circular cylinder. The variation of Strouhal number (St) with Re has also been discussed for different rectangular cylinders.

In flow past a fixed cylinder, the mode of vortex shedding is always antisymmetric, named the Karman street. However, with the cylinder oscillating in the streamwise direction, the mode of shedding can be either antisymmetric, symmetric or chaotic depending on the forcing parameters. Previous studies by Barbi *et al.* (1986) and Ongoren & Rockwell (1988) have found different antisymmetric and symmetric modes in these kinds of flows. Chaotic flow in the wake of an inline oscillating circular cylinder received renewed attention after its rediscovery by Perdikaris *et al.* (2009), who attributed it to mode competition between antisymmetric and symmetric modes, but the data presented by them do not indicate this.

In this thesis, we have reproduced all the symmetric modes reported in the literature, and also discovered a new symmetric mode, named S-III. To our knowledge, this is the first numerical study to report the S-II mode of vortex shedding. A study of occurrence of different modes for varying forcing frequency at fixed Re and A/D has been done, and it shown that different modes of shedding (antisymmetric, mixed, S-I, S-II, S-III) exist in different geometries. A physical mechanism based on ‘ground effect’ has been proposed to explain the S-II and S-III modes of shedding in tall cylinders. We also report chaotic flow for certain values of forcing frequency and amplitude, and show clear evidence that this is due to mode competition in the sense of Ciliberto & Gollub (1984), who were the first to report mode competition leading to chaos in another context.

Also, a Fourier-Spectral code developed to study the merger of vortices has been validated using existing results in the literature and some preliminary results have been presented.

Publications

Journal

- “Vortex shedding patterns, their competition, and chaos in flow past inline oscillating rectangular cylinders,” Srikanth T, Harish N Dixit, Rao Tatavarti & Rama Govindarajan, Accepted for Publication in the *Physics of Fluids*.
- “Vortex shedding from fixed tall rectangular cylinders,” Srikanth T, Harish N Dixit & Rama Govindarajan, *Manuscript under preparation*.

Proceeding

- “Shedding behaviour in flow past an inline oscillating square cylinder,” Srikanth T, Harish N Dixit & Rama Govindarajan, Proc. of the sixth IUTAM symposium on Bluff Body Wakes and Vortex Induced Vibrations (BBVIV-6), Capri Island, Italy, June 22-25, 2010.

Contents

Abstract	vii
1 Introduction	1
1.1 General	1
1.2 Vortex shedding from inline oscillating cylinders	2
1.3 Motivation and objectives of the study	6
2 The Lattice Boltzmann Method	9
2.1 The Lattice Boltzmann Method	9
2.2 Liouville equation, BBGKY hierarchy and the Boltzmann equation	9
2.3 The Lattice Boltzmann Equation	12
2.4 Euler and Navier-Stokes equations from the Lattice Boltzmann equation (LBE)	13
3 The Code and Its Validation	17
3.1 Computation domain and grid generation	17
3.2 Equations and boundary conditions	19
3.3 Code Validation	19
3.3.1 Fixed Cylinder	19
3.3.2 Inline Oscillating Cylinder	19
4 Results	23
4.1 Results	23
4.1.1 Fixed cylinders	23
4.1.2 Inline oscillating cylinders	26
5 Vortex Merger	39
5.1 Governing equations and the Fourier spectral method	39
5.2 Merger of same signed Gaussian vortices	41
5.2.1 Merger of two vortices: code validation	41
6 Conclusions	45
References	47

Chapter 1

Introduction

1.1 General

Vortex shedding from fixed cylinders has been extensively studied since at least the time of Vincenc Strouhal. An extensive survey of studies on vortex shedding from fixed circular cylinders can be found in Williamson (2000). Understanding the stability of offshore structures was one of the main motivations for these studies in the 1970's. Vortex shedding in the case of a uniform flow past a fixed cylinder is always antisymmetric; and the stability of this spatial arrangement of vortices was analytically studied by Theodore von Kármán for the case of point vortices in an infinite domain. A particular lateral spacing of vortices was found to be the only stable configuration. The flow in the wake of the cylinder is characterized by two time scales: that of the flow and that of the shedding of vortices from the cylinder. The cylinder experiences both drag and lift forces, the latter being the result of formation of low pressure zones on the 'top' and 'bottom' surfaces alternately. Both drag and lift fluctuate about a mean value, which is nonzero for the former and zero for the latter.

The flow pattern changes with the Reynolds number (Re), which is defined as the ratio of inertial to viscous forces in a given flow. It is given by: $Re = UD/\nu$, where U and D are velocity and length scales in the problem respectively and ν is the kinematic viscosity of the fluid. In the case of a circular cylinder, the flow is steady for $Re \leq 48$ with two bubbles always attached to the cylinder. As Re is increased beyond this critical value, the flow in the wake undergoes a Hopf bifurcation, with an exponential increase in the amplitude for short times (Sreenivasan *et al.* (1987), Provansal *et al.* (1989)). This regime is governed by the Landau equation (Landau & Lifshitz (2005a)):

$$\frac{d|A(t)|}{dt} = \gamma|A(t)| - \alpha|A(t)|^3 + O(|A(t)|^5). \quad (1.1)$$

Here, $|A(t)|$ is the amplitude of the disturbance, γ is the growth rate and $\alpha (> 0)$ is the Landau constant. For very short times $|A| \gg |A|^3$, and hence the growth is exponential. However, for longer times, one has to take terms of higher order into account. In the limit of $t \rightarrow \infty$, the amplitude of the disturbance saturates, and is given by $|A_{max}| = \sqrt{2\gamma/\alpha}$ (Landau & Lifshitz (2005a)). γ is a function of only Re , and for small deviations of Re from Re_{cr} , we may write $\gamma \sim (Re - Re_{cr})$, where Re_{cr} is the critical value of Re for which the cylinder starts shedding. The growth rates obtained from experiments can be used to determine the Re_{cr} (Sreenivasan *et al.* (1987), Provansal *et al.* (1989)). The flow remains two-dimensional for upto $Re = 200$ (Williamson (2000)).

When the cylinder is forced to oscillate in the streamwise direction or when there is an oscillating flow at the inlet, the antisymmetric mode need not be the only mode of shedding. Experiments carried out by different investigators have shown that different symmetric modes exist in the above case. Another interesting phenomenon reported is that of lock-on. This refers to the entrainment of shedding frequency by the frequency of cylinder oscillation. The shedding frequency can either lock-on to the frequency of oscillation or on to its sub-harmonic, and whether, and to which frequency lock-on takes place strongly depends on the oscillation frequency. In this numerical study, different modes of vortex shedding, their competition and effects of this competition on the flow have been investigated.

1.2 Vortex shedding from inline oscillating cylinders

Griffin & Ramberg (1974) were one of the first to study vortex shedding from a streamwise oscillating circular cylinder placed in a uniform flow. The experiments were carried out at $Re = 190$. The two other non-dimensional numbers relevant to this study are the frequency ratio and the reduced velocity. The former is defined as the ratio of excitation frequency (f_e) to the frequency of shedding in the fixed cylinder case (f_o), and the latter is defined as the ratio of free stream velocity (U) to the velocity amplitude of oscillation of cylinder ($f_e D$). Two different regimes of synchronization were found when the frequency ratio was varied with the remaining two parameters fixed. In regime-I the frequency of vortex shedding was locked onto the frequency of cylinder oscillation, and in regime-II it was locked onto half the frequency of cylinder oscillation. The spatial arrangement of vortices was complex in regime-I, and in regime-II it resembled the arrangement in the wake of a cylinder oscillating in the transverse direction. Also, for f_e close to $2f_o$ the streamwise spacing between the vortices was found to decrease with increasing f_e .

Barbi *et al.* (1986) studied vortex shedding and lock-on in oscillatory flow past a fixed circular cylinder. The occurrence of lock-on was clearly demonstrated in their experiments. Power spectra for the cases of increasing frequency of cylinder oscillation showed that the shedding frequency is gradually entrained by the oscillation frequency. This study also reported the symmetric shedding mode, in which two vortices are shed at the same instant during a cycle, and frequency of vortex shedding coincided with the oscillation frequency.

Ongoren & Rockwell (1988) carried out a systematic study of vortex shedding from circular cylinders oscillating at an angle α ($0^\circ \leq \alpha \leq 90^\circ$) to the freestream velocity. The non-dimensional amplitude was fixed at 0.13 and the non-dimensional frequency was varied from 0.5 – 4. Four different types of antisymmetric shedding modes, named as A-I, A-II, A-III and A-IV, and a symmetric mode, named as S, were identified. The numbers indicate the number of vortices shed during a cycle of cylinder oscillation. A-I closely resembled the Kármán street, and one vortex was shed at each end during each cycle. The frequencies of shedding in A-II, A-III and A-IV modes were same as the oscillation frequencies of the cylinder (lock-on). A-III and A-IV involved pairs of counter-rotating vortices. In the S mode, two vortices were shed at the same instant during one period of cylinder oscillation. A-III, A-IV and S modes were observed only for $\alpha \neq 90^\circ$. Competition between antisymmetric and symmetric modes leading to switching of modes during an experiment was observed. Figure 1.1 shows different modes obtained for different frequency ratios at $Re = 855$, $A/D = 0.13$ and $f_e/f_o = 0.5 - 4$.

Xu *et al.* (2006) discovered a new symmetric mode, named S-II, in their experiments on flow past an inline oscillating circular cylinder. Two pairs of binary vortices were shed during each cycle of cylinder oscillation at the same instant, and the frequency of shedding was locked onto the frequency of oscillation. There was considerable reverse flow in the system which aided the formation of secondary vortices on the cylinder surface. These experiments were carried out at high values of Re , A/D and f_e/f_o . The lift force on the cylinder during symmetric shedding is zero due to the symmetry present. Figure 1.2 shows this new mode of symmetric shedding for $Re = 500$, $A/D = 0.5$ and $f_e/f_o = 1.74$.

In their experiments, Konstantinidis & Balabani (2007) found that the symmetric arrangement of vortices is, at least for small amplitudes, always unstable; and always gives way to an antisymmetric pattern downstream. Their study used an oscillatory flow at the inlet. Their spectra confirmed the occurrence of lock-on in symmetric shedding as previously reported by Barbi *et al.* (1986).

Comparatively fewer studies have been carried out using square cylinders. Mineswitsch *et al.* (1994) studied this problem using numerical simulation. Their results are for $Re = 200$. They identified three subregimes within the antisymmetric regime: 1. regime of superposition (low frequencies and amplitudes, and very high frequencies); 2. the lock-in regime ($1.6 \leq f_e/f_o \leq 2.4$); 3. the transition regime beyond lock-in (large amplitudes and frequencies). In the first

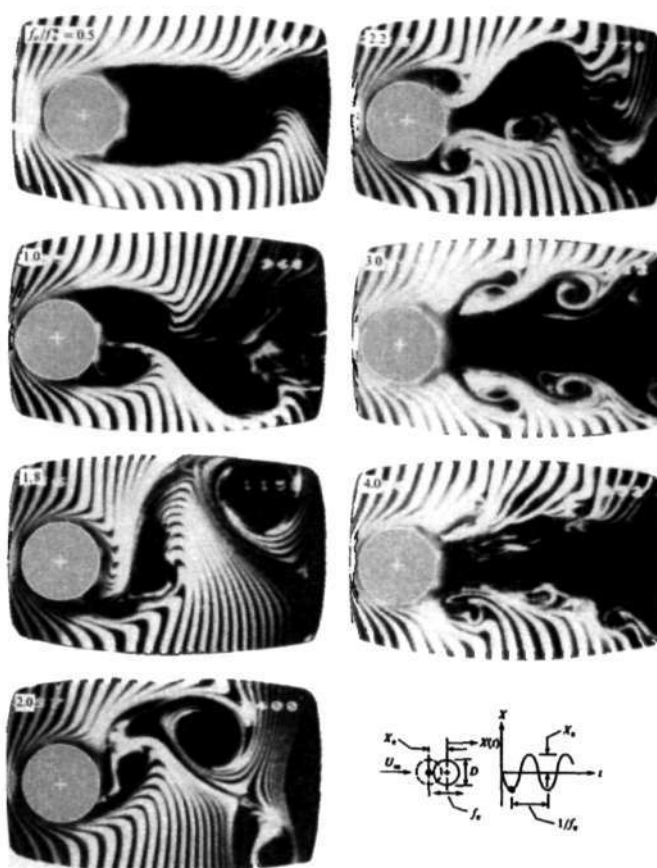


FIGURE 2. Preferred modes of near-wake structure for various ratios of excitation frequency f_e of cylinder to vortex shedding frequency f_o^* from corresponding stationary cylinder. All photos taken at instant when cylinder is in maximum upstream position during oscillation cycle.

Figure 1.1: Different modes of vortex shedding obtained by Ongoren & Rockwell (1988) for $Re = 855$, $A/D = 0.13$ and $f_e/f_o = 0.5 - 4$. The frequency ratio is increased from 0.5 to 4 as seen in the photos. The mode of shedding changes from antisymmetric ($f_e/f_o = 0.5$) to symmetric ($f_e/f_o = 3$). (Reproduced with permission from the *Cambridge University Press*)

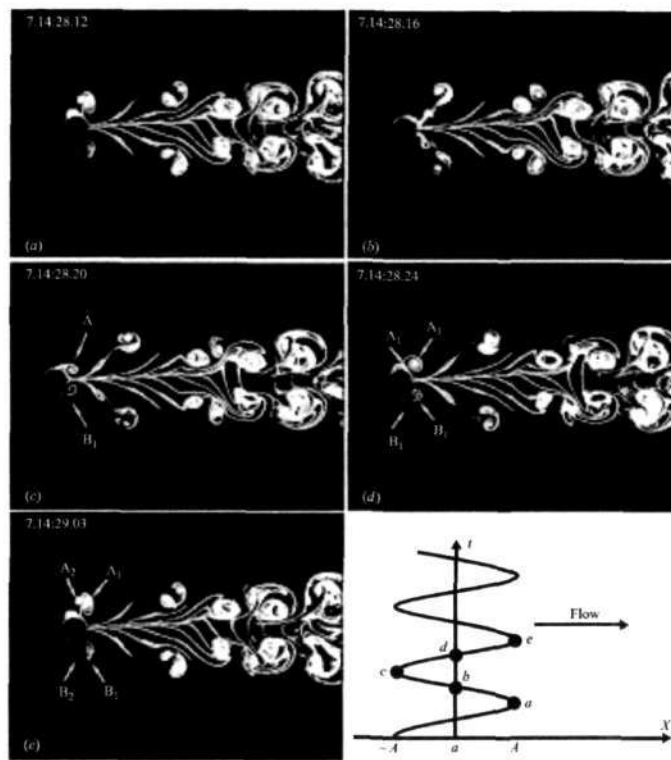


FIGURE 2. Sequential photographs of a symmetric binary vortex street at $f_e/f_o = 1.74$, $Re = 500$ and $A/d = 0.5$.

Figure 1.2: The S-II mode of vortex shedding discovered by Xu *et al.* (2006) for $Re = 500$, $A/D = 0.5$ and $f_e/f_o = 1.74$. Different phases during one period of cylinder oscillation are shown in the photos. As clearly seen, a pair of binary vortices is shed at the same instant during one period of oscillation. (Reproduced with permission from the *Cambridge University Press*)

regime, there was no interaction between vortex shedding and cylinder oscillation; the vortex shedding frequency was same as that of the corresponding fixed cylinder case. The vortex shedding frequency in the second regime adjusted itself such that $f_s = f_e/2$. In the third regime, symmetric structures were observed close to the cylinder. However, they were found to give way to antisymmetric street further downstream.

Table 1.1 lists the studies which have found symmetric shedding, and the list is not exhaustive.

Researchers	Re	f_e/f_o	A/D
King <i>et al.</i> (1973)	$5 - 15 \times 10^3$	2 - 4.2	0 - 0.2
Barbi <i>et al.</i> (1986)	40000	0.7	0.2
Couder & Basdevant (1986)	200	2	0.42
Ongoren & Rockwell (1988)	855	0.5 - 4	0.13
Detemple-Laake & Eckelman (1989)	152	1.4 - 1.7	NA
Okajima <i>et al.</i> (2000)	9000	2.4	0.08
Xu <i>et al.</i> (2006)	500	1.74	0.5
Konstantinidis & Balabani (2007)	1180 & 1240	3 - 4	0.02 & 0.04
Rao <i>et al.</i> (1992)	1000, 4000	2.5	0.2
Zhou and Graham (1992)	400 - 600	1.5 - 2.5	0.32 - 0.48

Table 1.1: Some of the studies (experimental and numerical) that have reported symmetric shedding (partly from Konstantinidis & Balabani (2007)). The first eight are experimental studies and the last two are numerical simulations.

In their numerical study on oscillatory flow, with no mean flow imposed, around a circular cylinder Vittori & Blondeaux (1993) reported chaotic flow, and they found that the route to chaos in their case was quasiperiodic. The two non-dimensional numbers, the Keulegan-Carpenter number ($Kc = U_o T/2a$) and the Reynolds number ($Re = 2aU_o/\nu$), were varied between 15.7 - 157 and 50 - 500 respectively. U_o is the velocity amplitude of inflow, T is the time period of inflow and a is the radius of the cylinder. For $Re \leq Re_{cr1}$, two bubbles were found attached to the cylinder during either half of the oscillation period. On further increase of the Re , the top-bottom symmetry was broken with the attached bubbles being of different strengths. When $Re \geq 250$, a "transverse sheet" mode was observed in which large vortex structures generated during each half cycle were found to move in a direction perpendicular to direction of mean flow. A secondary frequency was generated in this regime, which slowly increased in value with Re , and locked on to the primary frequency for $340 \leq Re \leq 370$. The flow was found to be chaotic for $370 \leq Re \leq 380$. On further increase in Re to 400, the flow was found to be primarily periodic again, but with spots of chaotic motion.

In a recent study, Perdikaris *et al.* (2009) found chaos in the wake of an inline oscillating circular cylinder in a uniform flow. Their computations were carried out for $Re = 400$ and $Re = 190$, but only the results in the former case were discussed. The cylinder underwent forced oscillations at the fixed Strouhal frequency with amplitude of oscillation being varied. The flow in the wake was chaotic for $0.18 \leq A/D \leq 0.23$, with antisymmetric shedding on either side of this range. Based on the spectra obtained, they surmised that the route to chaos was quasiperiodic and reason for the chaotic flow was competition between antisymmetric and symmetric modes of vortex shedding. However, the data was not conclusive to support their hypothesis that chaotic flow resulted due to mode competition. In chaos driven by mode competition, one would have intuitively expected that antisymmetric and symmetric modes would be dominant on either side of the chaotic window, but this was not observed. Conversely, the pattern was antisymmetric on either side of the chaotic window, which is not suggestive of mode competition. In fact all their spectra indicated antisymmetric shedding.



FIGURE 2. Optical intensity patterns for the (4, 3) and (7, 2) modes, respectively. The first index gives the number of angular maxima.

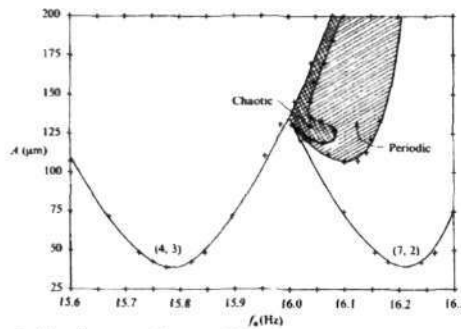


FIGURE 3. Phase diagram as a function of driving amplitude A and frequency f_0 . The crosses are experimentally determined points on the stability boundaries. Stable patterns occur in the regions labelled (4, 3) and (7, 2). Slow-periodic and chaotic oscillations involving competition between these modes occur in the shaded regions.

Figure 1.3: Mode competition in parametrically forced surface waves (Ciliberto & Gollub (1985)). A column of water was excited using sound waves from below, and different patterns formed were observed. Figure 2 in the photo shows the two different dominant modes, and Fig. 3 shows the chaotic window sandwiched between these two modes. (Reproduced with permission from the *Cambridge University Press*)

Chaos due to pattern competition is a general reason in many systems for the flow to become chaotic. This was discovered by Ciliberto & Gollub (Ciliberto & Gollub (1984), Ciliberto & Gollub (1985)) in their experiments on forced surface waves, where they observed chaotic windows sandwiched between two dominant modes. Water in a cylindrical container was subjected to small vertical oscillations. Chaos was found to occur at the intersection of stability curves of two different stable spatial patterns. Period-doubling bifurcations were observed, but the results were not conclusive enough to support this. Figure 1.3 shows these modes and the chaotic window.

1.3 Motivation and objectives of the study

The main motivation for this study is to understand the flow around an accelerating body. Sinusoidal variation of velocity is one of the simplest forms of acceleration, and this is the form used in this study. Inline oscillating rectangular cylinders are studied for the first time to our knowledge in this context. It is shown that the geometry has nontrivial effects on the flow field. This study is a first step towards understanding how the fluid flow changes when a body accelerates through it. This study has applications in tracking of submarine bodies.

In this study, vortex shedding from cylinders fixed in uniform and oscillatory flows has been studied numerically. The lattice Boltzmann equation is solved to obtain the flow parameters, and this numerical technique will be discussed in the next chapter. Different modes of vortex

shedding have been reproduced, and a new symmetric mode has also been discovered. A kinematic mechanism to explain the S-II mode in rectangular cylinders is proposed. It is shown that chaotic flow in the wake of a streamwise oscillating cylinder is indeed due to mode competition in the sense of Ciliberto & Gollub.

Chapter 2

The Lattice Boltzmann Method

Although the Lattice Boltzmann method (LBM) is available in a large volume of literature, the basic idea is sketched out here with the primary aim of making this thesis self contained. This discussion will hopefully provide important concepts regarding the LBM to a beginner. However, an expert on LBM may skip this chapter entirely.

2.1 The Lattice Boltzmann Method

LBM is one of the techniques used to simulate flow of a real fluid numerically. The lattice Boltzmann equation (LBE) is the discretized form of the discrete Boltzmann equation. Here, the discrete Boltzmann equation refers to the discrete set of velocities used in the Boltzmann equation; and the discretized form is the one in which both space and time have been discretized in the latter equation. The Boltzmann equation has been treated in great detail in the book by Harris (2004), and in the first chapter of “Physical Kinetics” by Landau-Lifshitz (Landau & Lifshitz (1981)). Discussions on LBM can be found in the books by Dieter A. Wolf-Gladrow (Wolf-Gladrow (2000)) and Sauro Succi (Succi (2006)), and in Chen & Doolen (1998). The LBE is an evolution equation for the velocity distribution function (f), with streaming and collision being the processes responsible for changes in f . Macroscopic flow quantities like density, velocity and energy can be obtained by taking appropriate moments of f . It will be described briefly in this chapter how the Navier-Stokes equation (NSE) is recovered from the LBE, with the BGK (Bhatnagar-Gross-Krook) approximation, in the limit of low Knudsen ($Kn = \lambda/L$) and low Mach numbers ($Ma = v/c_s$). Here, λ is the mean free path, L , v are the relevant length and velocity scales in the problem and c_s is the speed of sound.

There are advantages of solving the LBE over solving the NSE, the first one being the absence of nonlinearity in the convective term in the LBE. The velocity distribution in LBE is convected with particle speeds, which are constant. The equation is of course still nonlinear, but the nonlinearity is hidden in the approximate form of the collision integral. The second advantage is the ease with which an LBM code can be parallelized. And the third advantage is that the pressure is a local quantity in the LBM as the flow is weakly compressible, unlike in the incompressible NSE where pressure is a global quantity and a Poisson equation needs to be solved for it.

2.2 Liouville equation, BBGKY hierarchy and the Boltzmann equation

Statistical physics is the study of systems with very large degrees of freedom, usually $\sim 10^{23}$. In classical statistical physics, all molecules which make up the macroscopic system are assumed to obey Newton’s laws of motion. So, if we know the complete state of the system (positions and velocities of all molecules) at some initial time, then we can in principle determine the state of the system at some other time instant in future. However, as this involves solving a system of N , where $N \sim 10^{23}$, second order differential equations, this approach becomes impractical.

The state of a given system is advantageously described by representing it by a point in phase space or Γ -space. This has $6N$ axes representing $3N$ spatial coordinates (q_i , $i = 1, 2, \dots, N$) and $3N$ velocity components (p_i , $i = 1, 2, \dots, N$). Here, q_i and p_i are the position and velocity vectors of the i^{th} particle. As the molecules move about in time, the phase point moves about in this

phase space. To calculate the time average of a quantity one has to follow the system's behaviour in time, which can be impractical. To simplify this, an η number of different microscopic states (ensembles) which give rise to the same macroscopic state are considered, and these fill the phase space of the system. The positions and velocities of the particles in these η systems change with time, and to obtain the time-averaged value of a quantity one needs to find the average with respect to these η states (ensemble average). This is the idea behind the Gibbs Ensemble. The density of these states in the phase space is described by a normalized density distribution, $f_N(\mathbf{q}, \mathbf{p}, t)$, which is the number of molecules per unit phase-space volume normalized by the total number of molecules. This distribution obeys the normalization condition:

$$\int f_N(\underline{q}, \underline{p}, t) \prod_i dq_i dp_i = 1. \quad (2.1)$$

Here, $\underline{q} = (q_1, q_2, \dots, q_N)$ and $\underline{p} = (p_1, p_2, \dots, p_N)$.

The description of microscopic motion is not inherently probabilistic, but as we work with incomplete information (initial conditions) to begin with, the description becomes probabilistic (Landau & Lifshitz (2005b)). Now, the advantage of using the ensemble is that to calculate the average of a quantity of the system one need not follow the evolution of system in time, but needs to consider the different microscopic states which would give rise to the same averaged value of the quantity. This is due to the *ergodic* hypothesis.

$$\langle g \rangle = \lim_{T \rightarrow \infty} \frac{1}{T} \int_0^T g(t) dt = \int g(t) f_N(\mathbf{q}, \mathbf{p}, t) d\mathbf{q} d\mathbf{p} \quad (2.2)$$

Liouville equation describes the evolution of this probability density in phase space. It has a form similar to that of the continuity equation of fluid dynamics, but with the velocity replaced by the velocity of phase space coordinates. Liouville equation is:

$$\frac{\partial f_N}{\partial t} + \nabla \cdot (\underline{w} f_N) = \frac{\partial f_N}{\partial t} + \left(\sum_{i=1}^N \dot{q}_i \cdot \frac{\partial f_N}{\partial q_i} + \sum_{i=1}^N \dot{p}_i \cdot \frac{\partial f_N}{\partial p_i} \right) + f_N \left(\sum_{i=1}^N \frac{\partial \dot{q}_i}{\partial q_i} + \sum_{i=1}^N \frac{\partial \dot{p}_i}{\partial p_i} \right) = 0. \quad (2.3)$$

Here, \underline{w} is the velocity in phase space. The motion of the particles of the system is governed by Hamilton's equations which are given by

$$\dot{q}_i = \frac{\partial H}{\partial p_i}; \quad \dot{p}_i = -\frac{\partial H}{\partial q_i}. \quad (2.4)$$

$H(\underline{q}, \underline{p})$ is the Hamiltonian of the system. Using these equations in eqn. 2.3 we get,

$$\frac{\partial f_N}{\partial t} + \left(\sum_{i=1}^N \dot{p}_i \cdot \frac{\partial f_N}{\partial q_i} + \sum_{i=1}^N \dot{q}_i \cdot \frac{\partial f_N}{\partial p_i} \right) = 0. \quad (2.5)$$

Equation 2.5 is the simplified form of Liouville equation. This equation contains more information than needed to describe the system at the macroscopic level, and the parameters of interest depend only on far fewer degrees of freedom. Hence, we make use of reduced distribution functions. An R -particle ($R < N$) distribution function is defined as:

$$f_R = \frac{N!}{(N-R)!} \int f_N(q_1, \dots, q_N, p_1, \dots, p_N, t) \prod_{i=R+1}^N dq_i dp_i. \quad (2.6)$$

The factor $N!/(N-R)!$ represents the ways in which R particles can be chosen from N particles. f_R is the probability distribution in $6R$ dimensions in the Γ -space. Now, multiplying eqn. 2.5 by $\prod_{i=R+1}^N dq_i dp_i$ and integrating we obtain, after some algebra, the equation:

$$\frac{\partial f_R}{\partial t} + \sum_{i=1}^R \frac{\underline{p}_i}{m} \cdot \frac{\partial f_R}{\partial \underline{q}_i} - \sum_{i,j=1}^R \frac{\partial \phi_{ij}}{\partial \underline{q}_i} \cdot \frac{\partial f_R}{\partial \underline{p}_i} = (N-R) \int dx_{R+1} \sum_{i=1}^R \frac{\partial \phi_{iR+1}}{\partial \underline{q}_i} \cdot \frac{\partial f_{R+1}}{\partial \underline{p}_i}. \quad (2.7)$$

It is assumed that intermolecular forces between two molecules i and j can be represented using a two-particle potential ϕ_{ij} . So, $\underline{p}_i = -\sum_{j \neq i=1}^R \frac{\partial \phi_{ij}}{\partial \underline{q}_i}$. Equation 2.7 is called the BBGKY hierarchy of equations. These equations govern the evolution of an R -particle distribution function. However, these equations are not closed for a given R , and involve distribution functions of higher order as evident from the right hand side of eqn. 2.7. To solve for the R -particle distribution function one needs to know the $(R+1)$ -particle distribution function and so on. The Boltzmann equation is a single-particle distribution function, and is obtained from the BBGKY equations by putting $R = 1$ in eqn. 2.7. As mentioned before we have F_2 on the right hand side. The closed form of this equation was first obtained by Ludwig Boltzmann in 1872 by making the *stosszahlansatz* (molecular chaos assumption), according to which any two molecules entering a collision are not correlated before the collision, but are after it. Boltzmann used this to explain irreversibility in Nature, and through his famous *H-theorem* he showed that entropy of a system would always tend to increase. The Boltzmann equation was later derived more systematically from the BBGKY equation by Grad (Harris (2004)). The formal derivation of Boltzmann equation can be found in textbooks of Harris (2004) and Landau & Lifshitz (1981). The Boltzmann equation is:

$$\frac{\partial f}{\partial t} + \underline{v} \cdot \frac{\partial f}{\partial \underline{x}} = \int d\omega d\underline{v}_2 v_{rel} (f(\underline{x}, \underline{v}'_1, t) f(\underline{x}, \underline{v}'_2, t) - f(\underline{x}, \underline{v}_1, t) f(\underline{x}, \underline{v}_2, t)). \quad (2.8)$$

Here, $\underline{v}'_1, \underline{v}'_2$ and $\underline{v}_1, \underline{v}_2$ are the velocities of molecules involved in inverse and direct collisions respectively, $d\omega$ is the collision cross-section, $v_{rel} = |\underline{v}'_2 - \underline{v}'_1|$, is the relative speed of molecule 2 with respect to molecule 1 in the inverse collision. The conditions under which eqn. 2.8 is valid are (Harris (2004)):

- The gas is dilute, so that only binary collisions may be considered important.
- The properties of the gas depend slowly on spatial coordinates, so that the collisions can be considered as local events in physical space.
- The range of intermolecular forces is very small for the first two conditions to hold.

Maxwell obtained the equilibrium velocity distribution function based on isotropy arguments, and Boltzmann showed that Maxwell's distribution satisfied his equation (eqn. 2.8) and also that it is the *only* steady-state solution. The distribution is given by

$$f^{eq}(\underline{x}, \underline{v}, t) = \frac{\rho}{(2\pi RT)^{D/2}} \exp\left(-\frac{(\underline{v} - \underline{u})^2}{2RT}\right). \quad (2.9)$$

Here, ρ is the density of the fluid, $R (\equiv k_B/m)$ is the gas constant, k_B is the Boltzmann constant, T is the local temperature, D is the number of dimensions of space, \underline{v} is the velocity of a particle and \underline{u} is the macroscopic velocity of the fluid. If a system is not in local equilibrium, then the collision events bring the system back to local equilibrium. To simplify eqn. 2.8, Bhatnagar, Gross & Krook (Succi (2006)) approximated the collision integral to: $-(f - f^{eq})/\tau$, where f and f^{eq} are the nonequilibrium and equilibrium distribution functions respectively and τ is the collision time-scale. So, the Boltzmann equation with the BGK approximation reads:

$$\frac{\partial f}{\partial t} + \underline{v} \cdot \frac{\partial f}{\partial \underline{x}} = -\frac{1}{\tau} (f - f^{eq}). \quad (2.10)$$

Equation 2.10 seems linear, but the nonlinearity is hidden in f^{eq} . The macroscopic variables are given by the following formulae:

$$\rho(\underline{x}, t) = \int f(\underline{x}, \underline{v}, t) d\underline{v}; \quad (2.11)$$

$$\rho(\underline{x}, t)u(\underline{x}, t) = \int f(\underline{x}, \underline{v}, t)\underline{v}d\underline{v}; \quad (2.12)$$

$$\rho(\underline{x}, t)e(\underline{x}, t) = \int f(\underline{x}, \underline{v}, t)(\underline{v} - \underline{u})^2 d\underline{v}. \quad (2.13)$$

2.3 The Lattice Boltzmann Equation

If one uses a discrete set of velocities, eqn. 2.10 can be re-written as:

$$\frac{\partial f_i}{\partial t} + \underline{v}_i \cdot \frac{\partial f_i}{\partial \underline{x}} = -\frac{1}{\tau}(f_i - f_i^{eq}); \quad i = 0, 1, 2, \dots, S. \quad (2.14)$$

Here, S is the number of discrete velocity sets used. We choose U , L and n_r as the appropriate velocity, length and number-density scales in the problem. The convective time-scale then is L/U and let the collision time-scale be τ_c . Non-dimensionalizing eqn. 2.15 using these scales, we have $t' = tL/U$, $|v'_i| = |v_i|/U$, $|x'| = |x|/L$, $\tau' = \tau/\tau_c$, $\nabla' = L\nabla$ and $f'_i = f_i/n_r$. An important point to note is the different time scales used to non-dimensionalize the advection and collision processes. Using these we get,

$$\frac{\partial f'_i}{\partial t'} + \underline{v}'_i \cdot \frac{\partial f'_i}{\partial \underline{x}'} = -\frac{1}{\tau'Kn}(f'_i - f_i^{teq}); \quad i = 0, 1, 2, \dots, S. \quad (2.15)$$

$Kn (= \tau_c U/L)$ is the ratio of the mean-free path to the characteristic length scale in the problem. In the continuum regime, $Kn \rightarrow 0$. Here it is treated as a small parameter as we are interested in the continuum regime. Let $|\Delta \underline{x}'|$ and $\Delta t'$ be the non-dimensional grid-spacing and time step. If one chooses the particle velocity to be $\underline{v}'_i = \Delta \underline{x}'/\Delta t'$, the left hand side of eqn. 2.15 can be written as the total derivative along a characteristic line. This form can be discretized and written as

$$f'_i(\underline{x}' + \underline{v}'_i \Delta t', t' + \Delta t') - f'_i(\underline{x}', t) = -\frac{\Delta t'}{\tau'Kn}(f'_i - f_i^{teq}). \quad (2.16)$$

Using the form of Kn , we finally have

$$f'_i(\underline{x}' + \underline{v}'_i \Delta t', t' + \Delta t') - f'_i(\underline{x}', t) = -\frac{\Delta t}{\tau}(f'_i - f_i^{teq}). \quad (2.17)$$

Here, Δt and τ are dimensional quantities. Equation 2.17 is called the lattice Boltzmann equation with the BGK approximation.

Now, for $D = 2$, we can write the equilibrium distribution 2.9 as

$$f^{eq}(\underline{x}, t) = \frac{\rho}{(2\pi RT)} \exp\left(-\frac{\underline{v}^2}{2RT}\right) \exp\left(-\frac{\underline{u}^2 - 2\underline{v}\cdot\underline{u}}{2RT}\right). \quad (2.18)$$

Assuming the low Mach number limit, the last term on the right hand side of 2.18 can be expanded in Taylor series to upto $O(u^2)$ (He *et al.* (1996)). This gives

$$f^{eq}(\underline{x}, t) = \frac{\rho}{(2\pi RT)} \exp\left(-\frac{\underline{v}^2}{2RT}\right) \left(1 + \frac{\underline{v}\cdot\underline{u}}{RT} + \frac{(\underline{v}\cdot\underline{u})^2}{2(RT)^2} - \frac{u^2}{2RT}\right). \quad (2.19)$$

If one uses a nine-velocity model in two dimensions, it is called the D2Q9 (dimensions-2 and velocities-9) model. The velocities in a Cartesian co-ordinate system are given by

$$\underline{v}_i = \begin{cases} 0; & \text{if } i = 0 \\ c(\cos(i-1)\pi/2, \sin(i-1)\pi/2); & i = 1, 2, 3, 4 \\ \sqrt{2}c(\cos(i-5)\pi/2 + \pi/4, \sin(i-5)\pi/2 + \pi/4); & i = 5, 6, 7, 8. \end{cases}$$

In the D2Q9 model, one has evaluate integrals of the form:

$$I_m = \int_{-\infty}^{\infty} \exp(-x^2)x^m dx, \quad (2.20)$$

for calculating different moments of f , which give the macroscopic variables. In integrals of the form 2.20, x is a function of particle speed i.e., $x = g(v_i)$, and these can be evaluated using third order Hermite polynomial (He *et al.* (1996)). For an integral of the general form

$$I_m = \int_{-\infty}^{\infty} \exp(-x^2)f(x)dx, \quad (2.21)$$

the polynomial approximation is given by

$$I_m = \int_{-\infty}^{\infty} \exp(-x^2)f(x)dx \approx \sum_{i=1}^3 w_i f(x_i). \quad (2.22)$$

Here x_i 's are the roots of the third order Hermite polynomial (H_3) and w_i 's are the coefficients which are given by

$$w_i = \frac{2^{n+1}n!\sqrt{\pi}}{(H_{n+1}(x_i))^2}, \quad n = 3. \quad (2.23)$$

The third and fourth order Hermite polynomials are given by

$$H_3(x) = 8x^3 - 12x; \quad H_4(x) = 16x^4 - 48x^2 + 12. \quad (2.24)$$

Solving these we get: $x_1 = -\sqrt{3/2}$, $x_2 = 0$, $x_3 = \sqrt{3/2}$, $w_1 = \sqrt{\pi}/6$, $w_2 = 2\sqrt{\pi}/6$ and $w_3 = \sqrt{\pi}/6$. Using these values and after a lot of algebra, f_i^{eq} for the D2Q9 model can be written as

$$f_i^{eq} = \frac{4}{9}\rho \left(1 - \frac{3u^2}{2c^2}\right), \quad i = 0; \quad (2.25)$$

$$f_i^{eq} = \frac{1}{9}\rho \left(1 + 3\frac{u \cdot c}{c^2} + \frac{9(u \cdot c)^2}{2c^4} - \frac{3u^2}{2c^2}\right), \quad i = 1, 2, 3, 4; \quad (2.26)$$

$$f_i^{eq} = \frac{1}{36}\rho \left(1 + 3\frac{u \cdot c}{c^2} + \frac{9(u \cdot c)^2}{2c^4} - \frac{3u^2}{2c^2}\right), \quad i = 5, 6, 7, 8. \quad (2.27)$$

Here, $RT = c_s^2 = c^2/3$. c is speed of integration and c_s is the speed of sound.

2.4 Euler and Navier-Stokes equations from the Lattice Boltzmann equation (LBE)

The Euler and Navier-Stokes equations can be recovered from the LBE by carrying out a multiple-scale analysis. A more detailed derivation can be found in the book of Wolf-Gladrow (2000). In this method, the nonequilibrium distribution function (f) is expanded in powers of Kn , which is treated as a small parameter. The leading-order term (f^{eq}) is the equilibrium distribution function and the higher order terms represent departures from the equilibrium state. The time scales and length scale are also separated in terms of "fast time-scale" and "slow

time-scale", where the former represents the streaming motion of particles on very short time scales and the latter represents processes like convection and diffusion which happen on large time scales. After separating the time and length scales, terms of the same order in Kn are equated which gives the Euler equation at the first order, and the NSE at the second order. The method is briefly described below.

The perturbation expansion of f is given by:

$$f_i = f_i^{(o)} + \epsilon f_i^{(1)} + \epsilon^2 f_i^{(2)} + \epsilon^3 f_i^{(3)} + O(\epsilon^4). \quad (2.28)$$

The expansion 2.28 is called the Chapman-Enskog expansion. Here, $f_i^{(o)}$ is the equilibrium distribution function, f_i^{eq} . The $f_i^{(k)}$'s, ($k = 1, 2, 3, \dots$) represent departures from the equilibrium and do not contribute to the mass, momentum and energy as these quantities are collisional invariants. So, we have

$$\sum_k f_i^{(k)} = \sum_k e_{ik} f_i^{(k)} = 0; k = 1, 2, 3, \dots \quad (2.29)$$

Now, expanding the left hand side of the eqn. 2.17 in Taylor series we have

$$\frac{\partial f_i}{\partial t} \Delta t + \frac{\partial f_i}{\partial \underline{x}} \cdot \underline{v}_i \Delta t + \frac{\partial^2 f_i}{\partial t^2} \frac{(\Delta t)^2}{2} + \frac{\partial^2 f_i}{\partial \underline{x} \partial \underline{x}} : \underline{v}_i \underline{v}_i \frac{(\Delta t)^2}{2} + \underline{v}_i \cdot \frac{\partial}{\partial t} \frac{\partial f_i}{\partial \underline{x}} (\Delta t)^2 + O(\Delta t)^3 = -\frac{\Delta t}{\tau} (f_i - f_i^{eq}). \quad (2.30)$$

Introducing two different time-scales, t_1 and t_2 and length scale x_1 ,

$$\frac{\partial}{\partial t} = \epsilon \frac{\partial}{\partial t_1} + \epsilon^2 \frac{\partial}{\partial t_2}; \quad \frac{\partial}{\partial \underline{x}} = \epsilon \frac{\partial}{\partial x_1}. \quad (2.31)$$

Using 2.31 and 2.28 in eqn. 2.30 gives us (term by term):

$$\frac{\partial f_i}{\partial t} = \epsilon \left(\frac{\partial f_i^{eq}}{\partial t_1} \right) + \epsilon^2 \left(\frac{\partial f_i^{(1)}}{\partial t_1} + \frac{\partial f_i^{eq}}{\partial t_2} \right) + O(\epsilon^3); \quad (2.32)$$

$$\underline{v}_i \cdot \frac{\partial f_i}{\partial \underline{x}} = \epsilon \left(\underline{v}_i \cdot \frac{\partial f_i^{eq}}{\partial x_1} \right) + \epsilon^2 \left(\underline{v}_i \cdot \frac{\partial f_i^{(1)}}{\partial x_1} \right) + O(\epsilon^3); \quad (2.33)$$

$$\frac{\partial^2 f_i}{\partial t^2} = \epsilon^2 \left(\frac{\partial^2 f_i^{eq}}{\partial t_1^2} \right) + O(\epsilon^3); \quad (2.34)$$

$$\frac{\partial^2 f_i}{\partial \underline{x} \partial \underline{x}} : \underline{v}_i \underline{v}_i = \epsilon^2 \left(\frac{\partial^2 f_i^{eq}}{\partial x_1 \partial x_1} : \underline{v}_i \underline{v}_i \right) + O(\epsilon^3); \quad (2.35)$$

$$\underline{v}_i \cdot \frac{\partial}{\partial t} \frac{\partial f_i}{\partial \underline{x}} = \epsilon^2 \left(\underline{v}_i \cdot \frac{\partial}{\partial t_1} \frac{\partial f_i}{\partial x_1} \right) + O(\epsilon^3). \quad (2.36)$$

Using these in eqn. 2.30 gives

$$\begin{aligned} & \epsilon \Delta t \left(\frac{\partial f_i^{eq}}{\partial t_1} + \underline{v}_i \cdot \frac{\partial f_i^{eq}}{\partial x_1} \right) + \epsilon^2 \Delta t \left(\frac{\partial f_i^{(1)}}{\partial t_1} + \frac{\partial f_i^{eq}}{\partial t_2} + \underline{v}_i \cdot \frac{\partial f_i^{eq}}{\partial x_1} \right) + \\ & \epsilon^2 \Delta t^2 / 2 \left(\frac{\partial^2 f_i^{eq}}{\partial t_1^2} + \frac{\partial^2 f_i^{eq}}{\partial x_1 \partial x_1} : \underline{v}_i \underline{v}_i + \underline{v}_i \cdot \frac{\partial}{\partial t_1} \left(\frac{\partial f_i^{eq}}{\partial x_1} \right) \right) = -\frac{\Delta t}{\tau} \left(\epsilon f_i^{(1)} + \epsilon^2 f_i^{(2)} + O(\epsilon^3) \right). \end{aligned}$$

Comparing terms of $O(\epsilon)$, we have

$$E_1 \equiv \frac{\partial f_i^{eq}}{\partial t_1} + \underline{v}_i \cdot \frac{\partial f_i^{eq}}{\partial \underline{x}_1} + \frac{1}{\tau} f_i^{(1)} = 0. \quad (2.37)$$

The condition of conservation of mass is imposed by requiring that $\sum_i E_i = 0$, which gives

$$\sum_i \left(\frac{\partial f_i^{eq}}{\partial t_1} + \underline{v}_i \cdot \frac{\partial f_i^{eq}}{\partial \underline{x}_1} + \frac{1}{\tau} f_i^{(1)} \right) = \frac{\partial \rho}{\partial t_1} + \frac{\partial \rho u_k}{\partial x_k} = 0. \quad (2.38)$$

Equation 2.38 is the continuity equation. $f_i^{(1)}$ does not contribute to the mass by definition. Equation for momentum conservation can be obtained by taking the first moment of E_1 with respect to \underline{v}_i , i.e., $\sum_i E_i v_{ik} = 0$. So,

$$\sum_i \underline{v}_i \left(\frac{\partial f_i^{eq}}{\partial t_1} + \underline{v}_i \cdot \frac{\partial f_i^{eq}}{\partial \underline{x}_1} + \frac{1}{\tau} f_i^{(1)} \right) = 0. \quad (2.39)$$

The first term gives $\frac{\partial(\rho \underline{u})}{\partial t_1}$, and the form of f_i^{eq} is needed to evaluate the second term. This is where the form of equilibrium distribution becomes important as it leads to the correct form of momentum flux density tensor. The second term can be written as $\frac{\partial(\sum_i \underline{v}_{ij} v_{ik} f_i^{eq})}{\partial x_k}$. The general form of f_i^{eq} is given by

$$f_i^{eq} = \frac{W_i}{\rho_0} \left(\rho + \frac{m}{k_B T} (\underline{v}_i \cdot \underline{j}) + \frac{m}{2\rho k_B T} \left(\frac{m}{k_B T} (\underline{v}_i \cdot \underline{j})^2 - \underline{j}^2 \right) \right). \quad (2.40)$$

Here W_i 's are the weights as found in the subsection 2.3 and \underline{j} is the macroscopic momentum per unit volume. We now evaluate the contribution of second part term by term:

$$P_1 = \frac{\rho}{\rho_0} \sum_i W_i v_{i\alpha} v_{i\beta} = \frac{\rho}{\rho_0} \left(\frac{\rho_0 c^2}{3} \delta_{\alpha\beta} \right) = \frac{\rho c^2}{3} \delta_{\alpha\beta} = p(\text{say}). \quad (2.41)$$

The contribution of the second term is zero as it involves summation over an odd number of terms in \underline{v}_i , i.e., $\sum_i W_i v_{i\alpha} v_{i\beta} v_{i\gamma}$. So, $P_2 = 0$. Now, the term gives

$$P_3 = \frac{m}{2\rho\rho_0 k_B T} \frac{m}{k_B T} \sum_i W_i v_{i\alpha} v_{i\beta} v_{i\gamma} v_{i\delta} u_\gamma u_\delta = \frac{1}{2\rho} \left(\frac{m}{k_B T} \right)^2 \left(\frac{k_B T}{m} \right)^2 u_\gamma u_\delta T_{\alpha\beta\gamma\delta}. \quad (2.42)$$

$T_{\alpha\beta\gamma\delta} = \delta_{\alpha\beta} \delta_{\gamma\delta} + \delta_{\alpha\gamma} \delta_{\beta\delta} + \delta_{\alpha\delta} \delta_{\beta\gamma}$ is the fourth order isotropic tensor. Using this to evaluate the above expression, we obtain

$$P_3 = \frac{\rho}{2} u^2 \delta_{\alpha\beta} + \rho u_\alpha u_\beta. \quad (2.43)$$

Similarly, evaluating the last term we get $P_4 = -\frac{\rho}{2} u^2 \delta_{\alpha\beta}$. Adding all the P_i 's, we get the contribution as:

$$P_{\alpha\beta} = p \delta_{\alpha\beta} + \rho u_\alpha u_\beta. \quad (2.44)$$

Hence, the momentum equation in this case becomes:

$$\frac{\partial(\rho u_i)}{\partial t_1} + \frac{\partial(\rho u_i u_k)}{\partial x_{1k}} = -\frac{\partial p}{\partial x_{1i}}. \quad (2.45)$$

Equation 2.45 is the Euler equation which governs the motion of an ideal fluid. Now, to derive the correction to the stress tensor, one has to take the departure from equilibrium into consideration. All terms of $O(u^2)$ have been neglected in f_i^{eq} when evaluating the terms below. Hence, the below analysis is valid for only small Ma . Collecting all terms of $O(\epsilon^2)$ in eqn. 2.37 gives

$$\left(\frac{\partial f_i^{(1)}}{\partial t_1} + \frac{\partial f_i^{eq}}{\partial t_2} + \underline{v}_i \cdot \frac{\partial f_i^{eq}}{\partial \underline{x}_1} \right) + \frac{\Delta t}{2} \left(\frac{\partial^2 f_i^{eq}}{\partial t_1^2} + \frac{\partial^2 f_i^{eq}}{\partial x_1 x_1} : \underline{v}_i \underline{v}_i + 2 \underline{v}_i \cdot \frac{\partial}{\partial t} \frac{\partial f_i^{eq}}{\partial \underline{x}_1} \right) = -\frac{1}{\tau} f_i^{(2)}. \quad (2.46)$$

Again, evaluating the first moment of the eqn. 2.46 term by term, we have

$$\sum_i v_{i\alpha} \frac{\partial f_i^{(1)}}{\partial t_1} = 0; \quad \sum_i v_{i\alpha} \frac{\partial f_i^{eq}}{\partial t_2} = \frac{\partial(\rho u_\alpha)}{\partial t_2}; \quad (2.47)$$

$$\sum_i v_{i\alpha} v_{i\beta} \frac{\partial f_i^{eq}}{\partial x_{1\beta}}. \quad (2.48)$$

To evaluate the above term, the relation obtained for $f_i^{(1)}$ in terms of derivatives of f_i^{eq} in eqn. 2.37 is used. After some algebra, one obtains

$$\sum_i v_{i\alpha} v_{i\beta} \frac{\partial f_i^{eq}}{\partial x_{1\beta}} = -\tau \left(\frac{\partial}{\partial x_{1\beta}} \frac{\partial}{\partial t_1} \left(\sum_i v_{i\alpha} v_{i\beta} f_i^{eq} \right) + \frac{\partial}{\partial x_{1\beta}} \frac{\partial}{\partial x_{1\gamma}} \left(\sum_i v_{i\alpha} v_{i\beta} v_{i\gamma} f_i^{eq} \right) \right). \quad (2.49)$$

Considering the next term and noting that $\frac{\partial(\rho u_\alpha)}{\partial t_1} = -\frac{\partial P_{\alpha\beta}}{\partial x_{1\beta}}$, we obtain

$$\frac{\Delta t}{2} \sum_i v_{i\alpha} \frac{\partial^2 f_i^{eq}}{\partial t_1^2} = -\frac{\Delta t}{2} \frac{\partial}{\partial t_1} \sum_i \frac{\partial P_{\alpha\beta}}{\partial x_{1\beta}} \approx -\frac{\Delta t}{2} \frac{c^2}{3} \frac{\partial}{\partial t_1} \sum_i \rho \delta_{\alpha\beta}. \quad (2.50)$$

The above term, using the continuity equation is simplified to

$$\frac{\Delta t}{2} \sum_i v_{i\alpha} \frac{\partial^2 f_i^{eq}}{\partial t_1^2} = \frac{\Delta t}{2} \frac{c^2}{3} \frac{\partial}{\partial x_{1\alpha}} \frac{\partial}{\partial x_{1\gamma}} (\rho u_\gamma). \quad (2.51)$$

Similarly, the remaining two terms give

$$\frac{\Delta t}{2} \sum_i v_{i\alpha} v_{i\beta} v_{i\gamma} \frac{\partial}{\partial x_{1\beta}} \frac{\partial f_i^{eq}}{\partial x_{1\gamma}} = \frac{\Delta t}{2} \frac{\partial}{\partial x_{1\beta}} \frac{\partial}{\partial x_{1\gamma}} \left(\sum_i v_{i\alpha} v_{i\beta} v_{i\gamma} f_i^{eq} \right); \quad (2.52)$$

$$\Delta t \sum_i v_{i\alpha} v_{i\beta} v_{i\gamma} \frac{\partial}{\partial t_1} \frac{\partial f_i^{eq}}{\partial x_{1\beta}} = \Delta t \frac{\partial}{\partial x_{1\beta}} \frac{\partial}{\partial t_1} \left(\sum_i v_{i\alpha} v_{i\beta} f_i^{eq} \right). \quad (2.53)$$

Adding all these terms and using the same analysis used in deriving the Euler equation (and a little algebra too), one obtains

$$\frac{\partial(\rho u_\alpha)}{\partial t_2} = \left(\tau - \frac{\Delta t}{2} \right) \frac{c^2}{3} \left(\frac{\partial}{\partial x_{1\alpha}} \frac{\partial(\rho u_\beta)}{\partial x_{1\beta}} + \frac{\partial}{\partial x_{1\beta}} \frac{\partial(\rho u_\alpha)}{\partial x_{1\beta}} \right). \quad (2.54)$$

Adding the $O(\epsilon)$ and $O(c^2)$ terms, one gets the full Navier-Stokes equation.

$$\frac{\partial(\rho \underline{u})}{\partial t} + \frac{\partial(\rho \underline{u} \underline{u})}{\partial \underline{x}} = -\frac{\partial p}{\partial \underline{x}} + \nu \left(\frac{\partial^2 \rho \underline{u}}{\partial \underline{x} \cdot \partial \underline{x}} + \frac{\partial}{\partial \underline{x}} \frac{\partial}{\partial \underline{x}} \cdot (\rho \underline{u}) \right). \quad (2.55)$$

Here, $\nu = \left(\tau - \frac{\Delta t}{2} \right) \frac{c^2}{3}$, and the shear and bulk viscosities are the same. In the present code $\Delta t = 1$ and $c = 1$, so $\nu = \frac{1}{3} \left(\tau - \frac{1}{2} \right)$. The code is stable only when $\tau > 0.5$, which ensures positive kinematic viscosity.

Chapter 3

The Code and Its Validation

In this chapter the following aspects of the numerical code are briefly discussed: grid generation, equations solved, boundary conditions used and code validation. A nonuniform grid was used for computations, and as the LB method is for uniform grids some interpolation scheme is required to obtain the values of distribution functions at the nodes of the nonuniform grid. The algorithm for this can be found in He & Luo (1997).

3.1 Computation domain and grid generation

A domain size of $75D \times 75D$, where D is the height of the cylinder, with nonuniform grid was used for all cases. In this study the aspect ratio of a rectangular cylinder is defined as D/h , where h is the width of the cylinder. The number of grid points used is close to a million in most of the cases, and these numbers were arrived at after carrying out grid and domain independence studies. Schematics of the domain and grid used are shown in figs. 3.1(a) and 3.1(b).

The nonuniform grid is generated in the following way: The number of grid points per unit length is taken as N_{char} and the number of points on each side of the cylinder is calculated as $L \times N_{char}$, where L is D or h as appropriate. The uniform grid spacing is given by $\Delta x = \Delta y = 1/N_{char}$. Four layers of uniform grid are generated on each side of the cylinder with the values of Δx and Δy calculated above. The following variables are used:

- N_x and N_y , the total number of grid points in x- and y-directions respectively.
- (x_1, y_1) and (x_2, y_2) , the coordinates of the bottom left and top right corner points of the rectangular cylinder.
- (x_{1d}, y_{1d}) and (x_{2d}, y_{2d}) , the coordinates of the bottom left and top right corner points of the computation domain.
- $x_a = x_1 - 4\Delta x$, $x_b = x_2 + 4\Delta x$, $y_a = y_1 - 4\Delta y$ and $y_b = y_2 + 4\Delta y$, the points upto which uniform grid is generated.
- N_x and N_y , the number of grid points in the bottom left part of the domain.
- r and Δr , stretching parameters. Here $r > 1$.

The following equation is solved iteratively to obtain the x-coordinates of the grid points:

$$x(i) = x(i-1) - r(x(i+2) - x(i+1)); \quad i = N_x - 3, N_x - 4, \dots, 1. \quad (3.1)$$

The above equation reduces to: $x(i) = x(i-1) + r\Delta x$. The value of r is arbitrarily assumed in the beginning and is corrected to ensure that there are N_x grid points in the region of interest. The correction is done using the relation: $r = r - 0.001 \times (\Delta r/N_x)$. As $r > 1$, one obtains grid stretching as one moves away from the cylinder. The same algorithm is used for other regions of the domain too. The total number of grid points used is from 5×10^5 (for a square cylinder) to $\approx 10^6$ (for rectangular cylinder of $D/h = 8$).

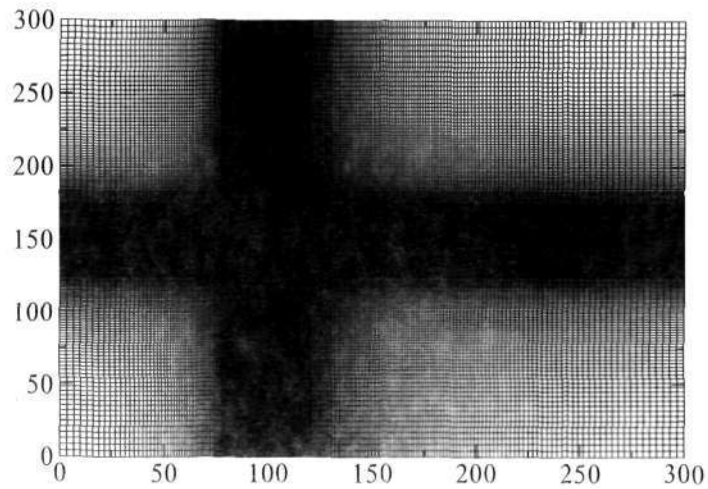
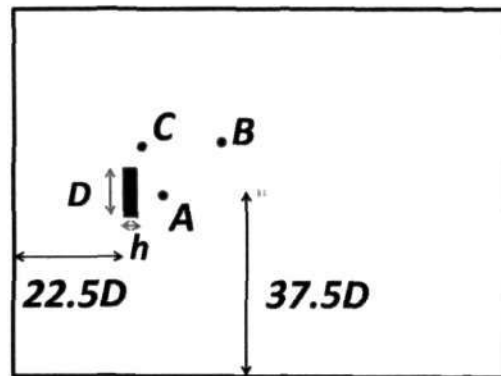


Figure 3.1: (a) Schematic of the domain used in the simulations. Time signals are stored at the monitor points A , B and C , located at $(2h, 0)$, (h, D) and $(2.25D, 0.5D)$ respectively (not to scale). (b) The grid used.

3.2 Equations and boundary conditions

The lattice Boltzmann equation given by:

$$f_i(\underline{x} + \underline{v}_i, t + 1) - f_i(\underline{x}, t) = -\frac{1}{\tau}(f_i - f_i^{eq}); \quad i = 0, 1, 2, \dots, 8, \quad (3.2)$$

is solved for the flow. The above equation is linear in f_i , but the nonlinearity is hidden in f_i^{eq} . This equation is supplemented by the equation for f_i^{eq} , which is given by:

$$f_i^{eq} = \frac{4}{9}\rho \left(1 - \frac{3}{2} \frac{u^2}{c^2}\right); \quad i = 0 \quad (3.3)$$

$$f_i^{eq} = \frac{1}{9}\rho \left(1 + 3 \frac{\underline{u} \cdot \underline{e}}{c^2} + \frac{9}{2} \frac{(\underline{u} \cdot \underline{e})^2}{c^4} - \frac{3}{2} \frac{u^2}{c^2}\right); \quad i = 1, 2, 3, 4 \quad (3.4)$$

$$f_i^{eq} = \frac{1}{36}\rho \left(1 + 3 \frac{\underline{u} \cdot \underline{e}}{c^2} + \frac{9}{2} \frac{(\underline{u} \cdot \underline{e})^2}{c^4} - \frac{3}{2} \frac{u^2}{c^2}\right); \quad i = 5, 6, 7, 8. \quad (3.5)$$

The macroscopic variables, ρ and \underline{u} , are found from f_i 's as discussed in the last chapter.

The following boundary conditions were used:

- $u = u_o + \Delta u \sin \omega t$ at the inlet and top and bottom surfaces of the domain.
- $\frac{\partial u}{\partial x} = \frac{\partial v}{\partial x} = 0$ at the outlet.
- $\underline{u} = 0$ on the cylinder.

In the LBM, the boundary conditions have to be applied via f_i . For the no-slip boundary condition, the bounce-back scheme is used, and for the slip condition the reflective boundary condition is used.

3.3 Code Validation

The code was validated for both fixed and oscillating cylinder cases. A square cylinder was used for validation as previous results for the same geometry are available in the literature.

3.3.1 Fixed Cylinder

For flow past a fixed square cylinder, Strouhal numbers, defined as $St = f_o D / U_\infty$ which is nondimensional frequency of shedding, obtained from the code were compared with the Strouhal numbers obtained from Okajima's (Okajima (1982)) experiments and Ansumali *et al.*'s (Ansumali *et al.* (2003)) numerical simulations. Figure 3.2 shows the comparison. As evident the results are in good agreement with experiment and with another numerical simulation.

The drag coefficients obtained for the fixed square cylinder case were compared with the drag coefficients obtained from Okajima *et al.* (1997) and Sharma & Eswaran (2004). The results obtained are in excellent agreement with Okajima's results for moderate Re . The comparison is shown in fig. 3.3. Also, the length of recirculation region, L , for the square cylinder is compared with those obtained by Sharma & Eswaran (2004). The comparison is shown in 3.4.

3.3.2 Inline Oscillating Cylinder

For the case of an inline oscillating square cylinder, the frequency response obtained from the present code was compared with that of Mineswitsch *et al.* (1994). The dominant frequencies in the spectrum for the wall normal velocity u_y at a typical location obtained from our simulations

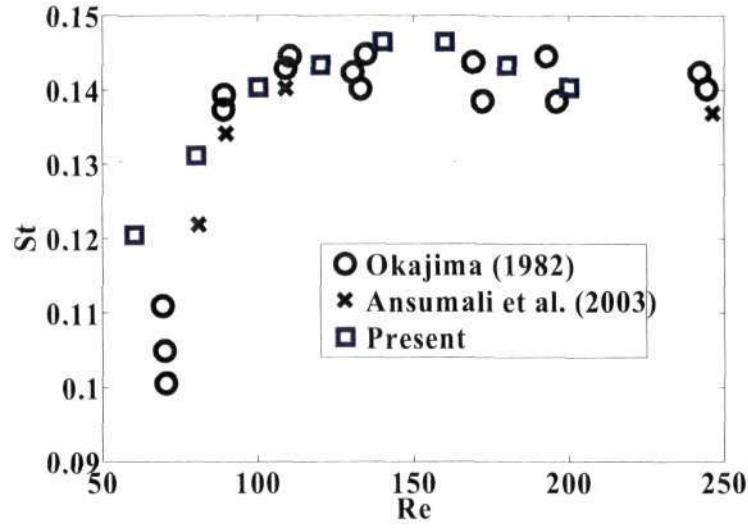


Figure 3.2: Comparison of Strouhal numbers obtained from experiment and numerical simulation. Squares: present study; circles: experimental data from Okajima (1982); and crosses: numerical simulation by Ansumali *et al.* (2003).

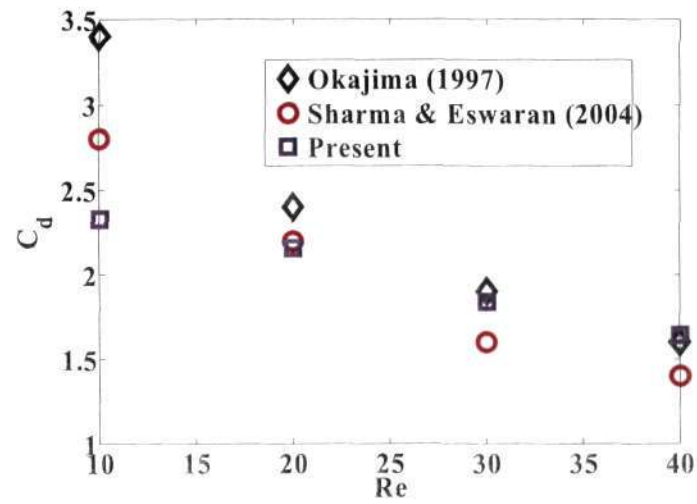


Figure 3.3: Comparison of C_d obtained from experiment and numerical simulation. Squares: present study; diamonds: experimental data from Okajima *et al.* (1997); and circles: numerical simulation by Sharma & Eswaran (2004).

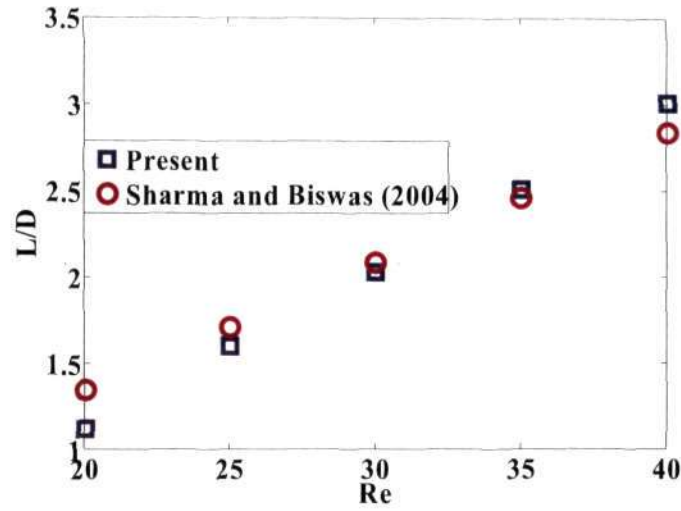


Figure 3.4: Comparison of length of recirculation region behind the square cylinder for $20 \leq Re \leq 40$ with Sharma & Eswaran (2004). The values obtained are clearly in good agreement.

agree very well with the spectrum for the lift coefficient obtained by Mineswitsch *et al.* (1994) for this geometry. This is shown in fig. 3.5. Also, as done in Mineswitsch *et al.* (1994), the frequency ratio was fixed at $f_e/f_o = 1.6$ and A/D was varied from 0.15 - 0.4 in steps of 0.05. The quantities f_e , f_o , A and D have been defined in the beginning of the first chapter. In excellent agreement with Mineswitsch *et al.* (1994), the lock-on window between $0.15 \leq A/D \leq 0.4$, where $f_s = 0.5f_e$ is reproduced.

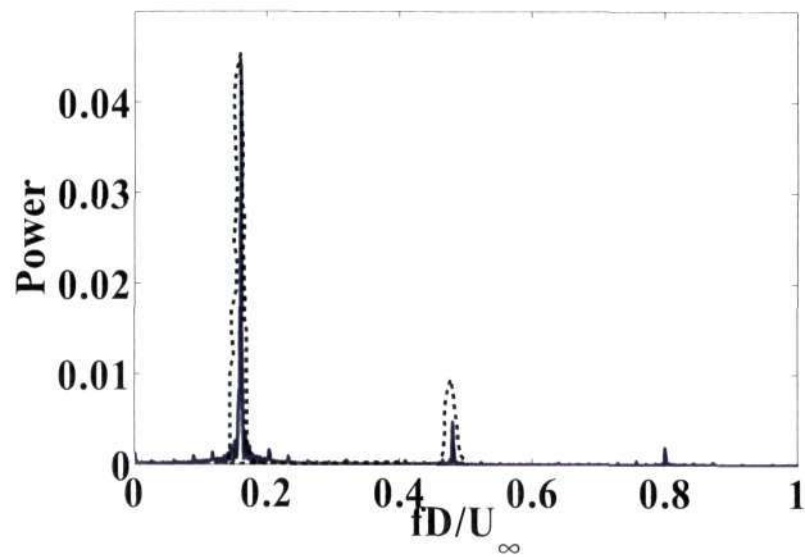


Figure 3.5: Comparison between the spectra obtained from Mineswitsch *et al.* (1994) (dashed line) and the present code (solid line) for $Re = 200$, $A/D = 0.25$ and $f_e = 0.32U_\infty/D$. The present spectrum is obtained from the time signal of u_y at monitor point A in fig. 3.1(a). The power spectrum of Minewitsch *et al.* is that of their lift coefficient, and has been arbitrarily scaled.

Chapter 4

Results

In this chapter, results obtained for the cases of fixed and oscillating rectangular cylinders are discussed. In the first section, the method used to calculate the critical Reynolds number is briefly discussed. The results obtained are in agreement with linear stability theory, which predicts a linear scaling between the disturbance growth rate, γ , and $(Re - Re_{cr})$ i.e., $\gamma \sim (Re - Re_{cr})$ when this difference is not too large. Also, Strouhal numbers, St , are obtained for different Re for two different geometries.

The second section contains discussions on different modes of vortex shedding, chaotic flow in the wake and different routes to chaos in the present problem of flow past an inline oscillating rectangular cylinder. The results of the parametric study are presented showing the occurrence of different modes of shedding for different forcing parameters. The $S - I$ and $S - II$ modes found in previous experiments have been reproduced here, and this is the first numerical study to report the $S - II$ mode. Also, a new symmetric mode, $S - III$, has been discovered, and is discussed in detail. It is also shown that the flow in the wake becomes chaotic for certain range of forcing parameters, and the routes could be competition between antisymmetric and symmetric modes of shedding or the well-known Ruelle-Takens route. An integrated quantity is used to 'quantify' the chaos in the system.

A part of the study has been accepted for publication in the *Physics of Fluids*.

4.1 Results

4.1.1 Fixed cylinders

For $Re < Re_{cr}$, the flow behind a fixed cylinder is steady and a recirculation bubble can be seen attached to the cylinder. This is shown in fig. 4.1. The length of this recirculation region, L , is defined as the distance from the rear of the cylinder to the saddle point in the wake region. In the case of a circular cylinder, the bubble becomes unstable and assumes a time varying wavy shape when $L/D \geq 2$. However, in the case of rectangular cylinders the bubble is stable even for $L/D > 3$ and becomes unstable only at higher L/D values. This indicates that the geometry of the body plays an important role in the stability of the attached bubble, and that $L/D \approx 2$ is not a universal value after which the instability in the wake sets in. Figure 4.2 shows how the bubble size varies with Re for cylinders of different aspect ratios. The values obtained for the square cylinder are in excellent agreement with the results of Sharma & Eswaran (2004).

Similar to the case of a circular cylinder, a Kármán street is observed for $Re > Re_{cr}$. However, there are slight differences between cylinders of different aspect ratios. Figures 4.3(a) - 4.3(d) show the Kármán streets for rectangular cylinders of aspect ratio 1, 2, 4 and 6.

In the cases where Re is slightly higher than Re_{cr} , the growth of a disturbance has three stages of development. In the first stage the disturbance grows exponentially with time; this is the linear regime. In the second stage, there is a transition from linear to nonlinear flow, and finally in the third, the disturbance reaches a saturated nonlinear state (H. Oertel (1990)). These regions are clearly seen in fig. 4.4. H. Oertel (1990) introduces an additional zeroth stage, where the disturbance is too small to detect.

To calculate the Re_{cr} for different cylinders, the method given in Sreenivasan *et al.* (1987) and Provansal *et al.* (1989) is used. As mentioned earlier, the Re at which the growth rate of disturbance, γ , is zero is the required critical Reynolds number. The growth rates can be found

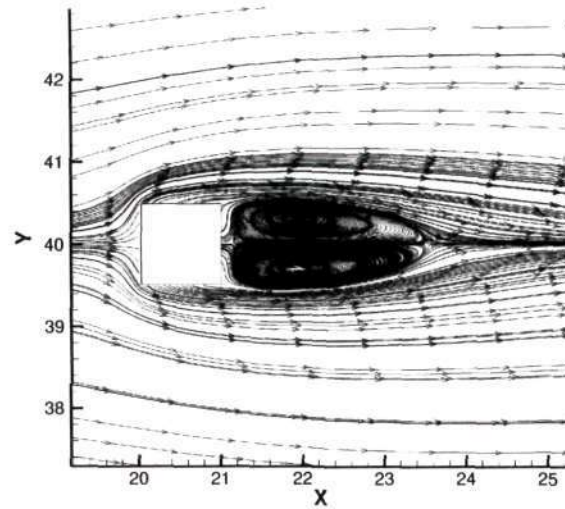


Figure 4.1: Wake behind the square cylinder for $Re = 30$. Two bubbles attached to the cylinder can be seen. The bubble length, L , is defined as the distance between the rear of cylinder and the saddle point in the wake. The apparent asymmetry is due to the manual selection of streamlines.

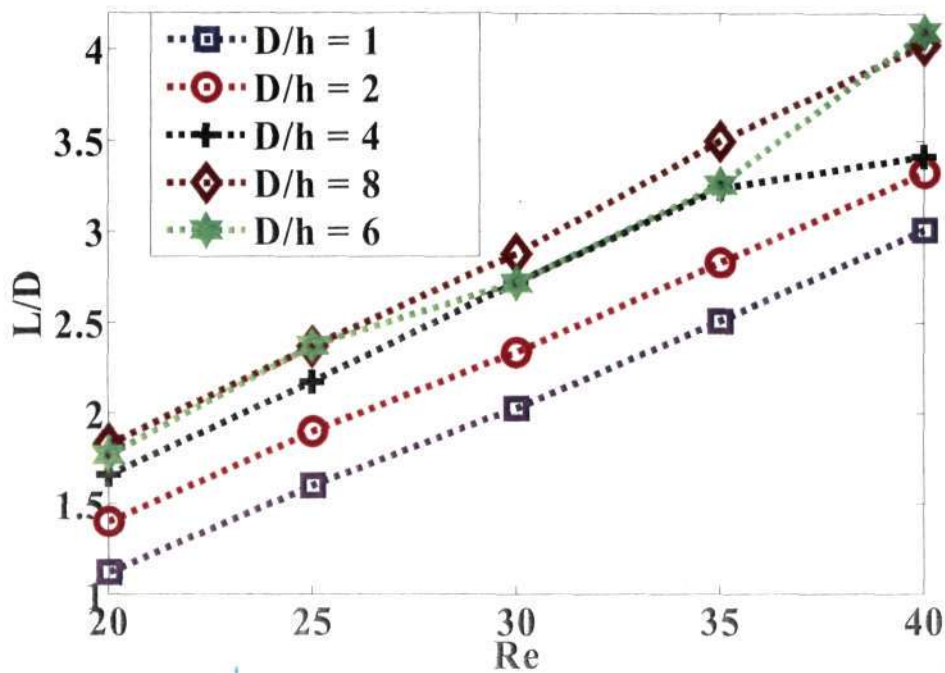


Figure 4.2: Bubble size (L/D) vs. Re for rectangular cylinders of different aspect ratios. As can be seen, the flow in the wake is stable even for $L/D > 3$ in all cases. The bubble sizes obtained for the square case ($D/h = 1$) are in excellent agreement with the values obtained by Sharma & Eswaran (2004). For the most part, the bubble size varies linearly with Re .

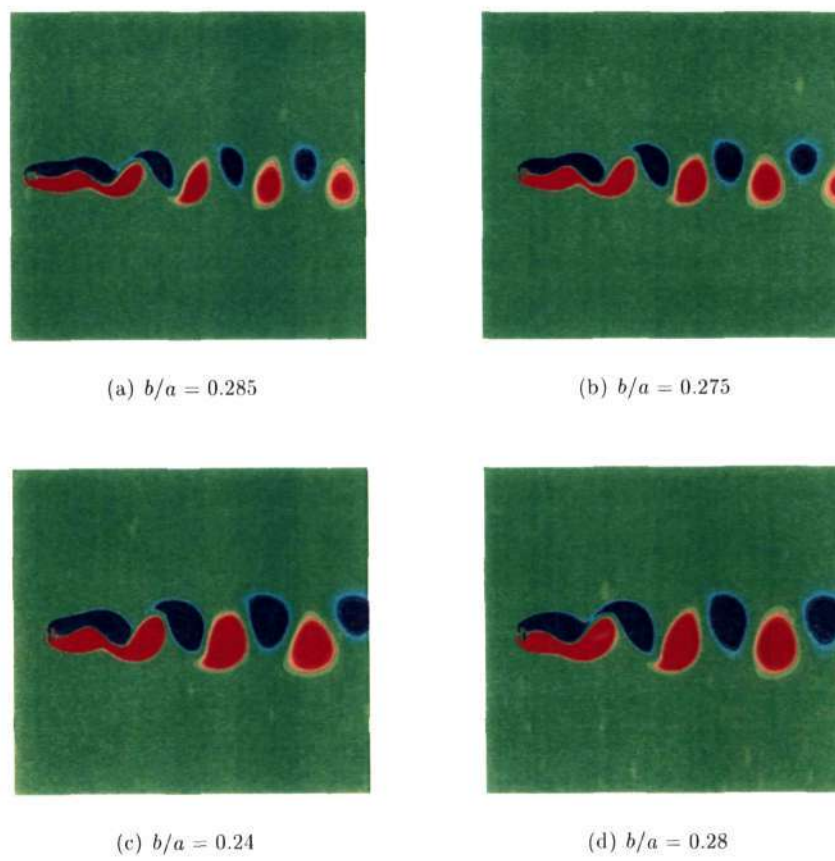


Figure 4.3: Kármán streets for (a) $D/h = 1$, (b) $D/h = 2$, (c) $D/h = 4$ and (d) $D/h = 6$. The ratio of transverse (b) and streamwise (a) distances (b/a) between two consecutive vortices is also shown.

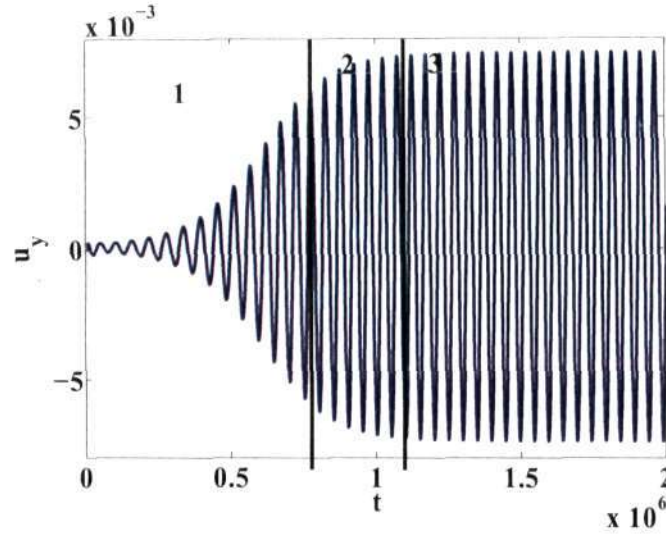


Figure 4.4: $D/h = 4$ and $Re = 40$. This plot shows the evolution of a disturbance in the wake for $Re > Re_{cr}$ and not very far from it. The zeroth region is not seen in this case. However, the other regions are discernible in the plot. Region-1: linear regime, region-2: region of transition and region-3: saturated nonlinear state.

from the time signals of, say u_y or C_L , and exponential curves of the form $u_y = ae^{\gamma t}$, where γ is the growth rate, can be fit to the amplitude in the early transient parts of the curves. For $Re < Re_{cr}$, $\gamma < 0$ which means that all disturbances are damped and for $Re > Re_{cr}$, $\gamma > 0$ showing the growth of the dominant disturbances. These values are plotted against Re and the intercept on the abscissa is found, which gives Re_{cr} . Figures 4.5(a) - 4.6(b) show the growth rates obtained from the time signals of u_y at the monitor point A behind the cylinders. Growth rates in both cases have been nondimensionalized using the inverse of respective convective time scales.

It is found that the growth rate, γ , for Re not very far from Re_{cr} indeed varies linearly as $(Re_{cr} - Re)$, as predicted by the linear theory. The range of linear behaviour is remarkably large, as is clearly seen in both figs. 4.5(a) - 4.6(b) and especially in the latter.

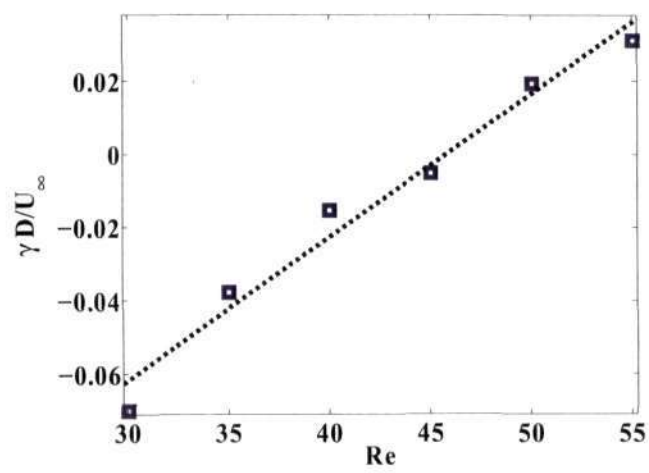
It is observed that Re_{cr} decreases slightly with increasing D/h , i.e. with increasing bluffness of the cylinder. This is intuitive as one would expect the instability to set in sooner for more blunt geometries. Re_{cr} is plotted against D/h as shown in fig. 4.7.

The Strouhal numbers for $D/h = 2, 4$ geometries have been obtained for $80 \leq Re \leq 200$. These are shown in figs 4.8(a) and 4.8(b).

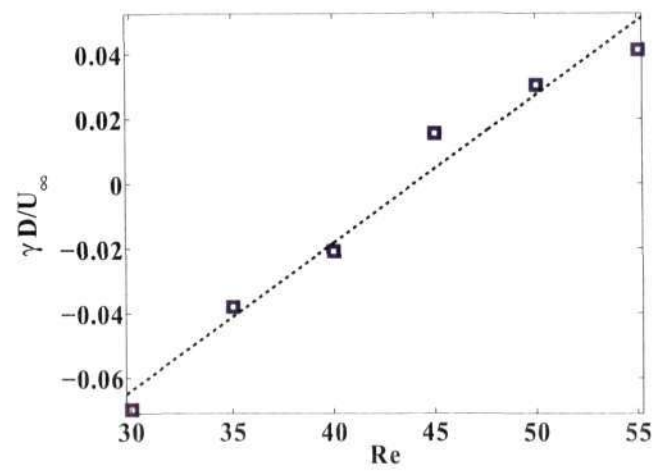
4.1.2 Inline oscillating cylinders

Modes of vortex shedding

When the oscillation frequency f_e is very small, the flow is not too different from that past a fixed cylinder, except that the Reynolds number now is slowly varying. One expects, and finds, a slightly modified Kármán street behind the body in this case. The same is true when the amplitude of oscillation A/D is small, since the oncoming flow merely sees a slightly modified body on an average. To observe competition between symmetric and antisymmetric shedding, one needs an effective oscillation Reynolds number $Re_o = (\Omega A)D/\nu$ which is not negligible compared to that of the incoming flow. Although we carried out many simulations to ensure that our results are general, we present only a few typical ones. The shedding pattern changes as the excitation frequency f_e is increased from $0.5f_o$, half the natural shedding frequency

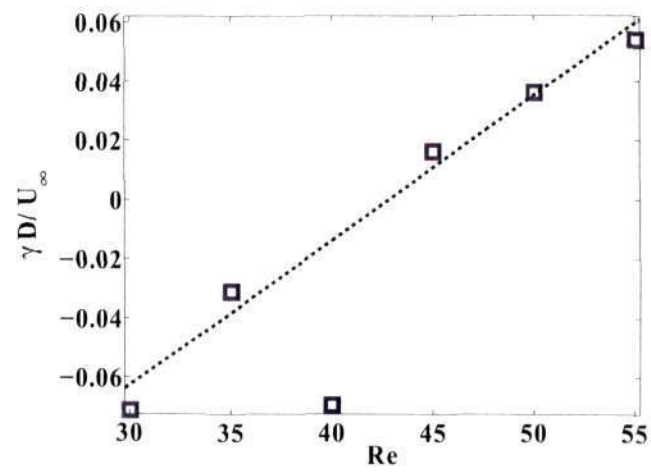


(a)

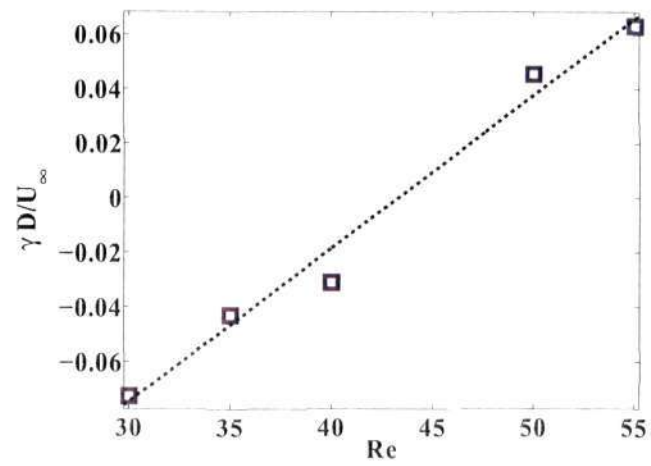


(b)

Figure 4.5: Calculation of Re_{cr} for $D/h = 1, 2$. The nondimensional growth rate, $\gamma^* = \gamma D/U_\infty$, is plotted against Re . (a) $Re_{cr} \approx 45.86$ and (b) $Re_{cr} \approx 44.03$



(a)



(b)

Figure 4.6: Calculation of Re_{cr} for $D/h = 4, 6$. Nondimensional growth rate, γ^* , is plotted against Re . (a) $Re_{cr} \approx 42.82$ and (b) $Re_{cr} \approx 43.3$

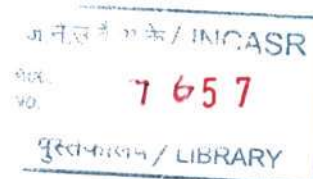
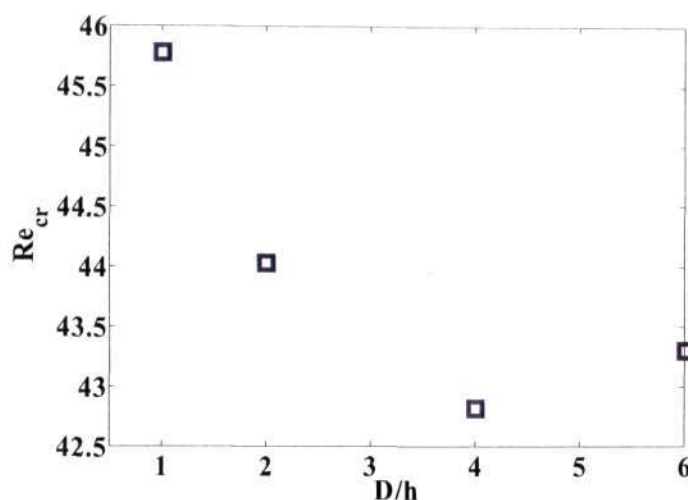


Figure 4.7: Plot showing variation of Re_{cr} with D/h . It is seen that there is a slight decrease in Re_{cr} with increasing D/h .

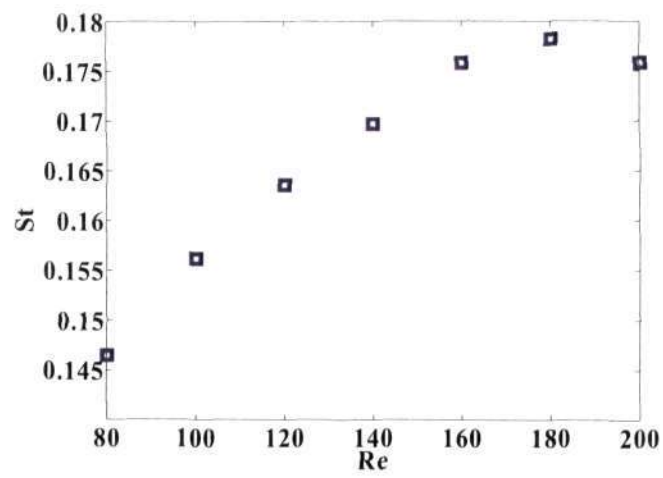
of a stationary cylinder, to five times this value, some examples are shown in figure 4.9. A rectangular cylinder of aspect ratio 4 is used here and A/D is fixed at 0.1. At low f_e the shedding is antisymmetric, and goes to symmetric shedding as f_e increases. At $f_e/f_o = 5$ we have the symmetric S-I mode, with all the top vortices being of one sign, and all the bottom of the opposite sign. At moderate f_e/f_o , the shedding is neither symmetric nor antisymmetric, but the upper and lower vortices are shed with a phase between 0 and π (or π and 2π). The flow however is still periodic. In some cases, vortex merger on each side of the cylinder is promoted, and the pattern downstream becomes antisymmetric. At small f_e , the shedding frequency f_s is close to f_o . However, as f_e/f_o is increased beyond 2, f_s decreases before locking on to a subharmonic of f_e , and then starts increasing proportionately with f_e , such that $f_s/f_e = 0.25$ for $3 \leq f_e/f_o \leq 4$. Beyond this range f_s steadily decreases with further increase in f_e . The lock-on is similar to those seen on circular cylinders Konstantinidis & Balabani (2007). Note that at these high frequencies shedding occurs on a given surface once every four complete oscillations, rather than once in every other oscillation.

Next, choosing $A/D = 0.175$, we summarise in figure 4.10 the patterns of vortex shedding observed on cylinders with aspect ratio $D/h = 1, 2, 4$ and 8. This higher oscillation amplitude will be seen to contrast with the lower A/D discussed above, in particular in the transition from an antisymmetric pattern of shedding to a symmetric. In the case of a square cross section, one would have to go to high amplitudes of oscillation to observe symmetric shedding. We benefit by the use of rectangular geometries, where a small oscillation amplitude is sufficient to observe different modes of shedding in the typical range of frequencies we use. The symmetric modes obtained may be classified into three types, S-I to S-III. As mentioned earlier, the first two have been observed in experiments before, but on circular cylinders (Ongoren & Rockwell (1988); Xu *et al.* (2006)). The letter S signifies a symmetric pattern, while the number denotes how many pairs of shed vortices may be associated with one time period of the flow. Thus the cylinder sheds one vortex of each sign both at the top and the bottom in an S-II mode. At higher oscillation frequencies, the flow displays what we term as a mixed mode.

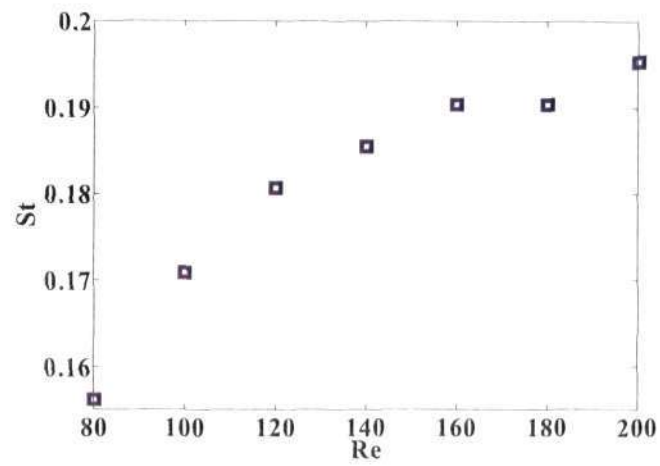
To discuss the mixed mode, shown in figure 4.11, we choose a square geometry. Such a pattern has also been seen by Konstantinidis & Balabani (2007). The shedding off the cylinder is actually symmetric, but some distance downstream, the shed vortices arrange themselves in an antisymmetric pattern, much like a Karman street, but with a larger spacing, and a correspondingly lower Strouhal number of 0.92 times that of a fixed square cylinder at this

621.437

P11



(a)



(b)

Figure 4.8: Plots showing the variation of St with Re for (a) $D/h = 2$ and (b) $D/h = 4$.

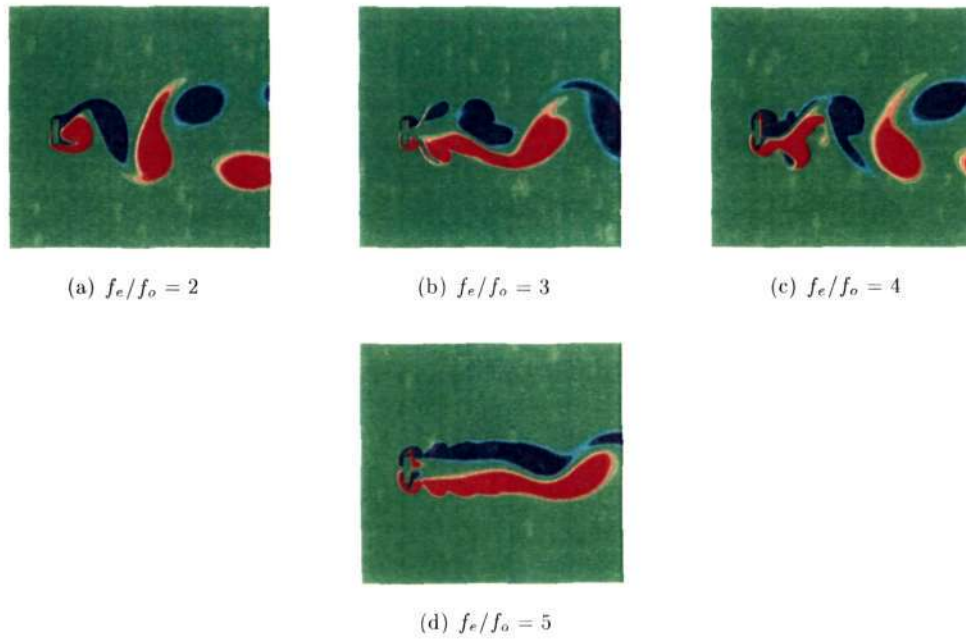


Figure 4.9: Vorticity fields at a typical time for $A/D = 0.1$ at various excitation frequencies for a cylinder of aspect ratio 4.

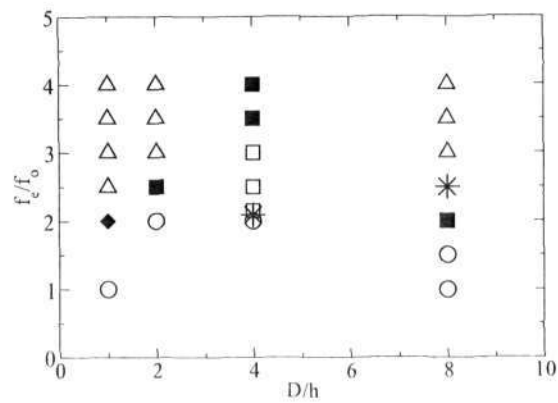


Figure 4.10: Flow patterns in the wake of an incline oscillating rectangular cylinder at $Re = 200$ and $A/D = 0.175$. Circles: antisymmetric shedding, squares: symmetric shedding. The solid squares indicate the S-II mode, the open squares stand for the S-I mode, while the patterned square indicates an S-III shedding. Triangles: mixed mode, where the shedding is symmetric but the vortices arrange themselves into an antisymmetric pattern downstream. Stars: chaotic flow, single solid diamond: the Couder-Basdevant mode.

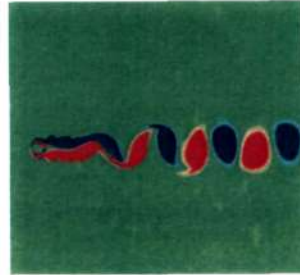


Figure 4.11: Mixed mode in the case of square cylinder, $f_e/f_o = 4$, $A/D = 0.175$.

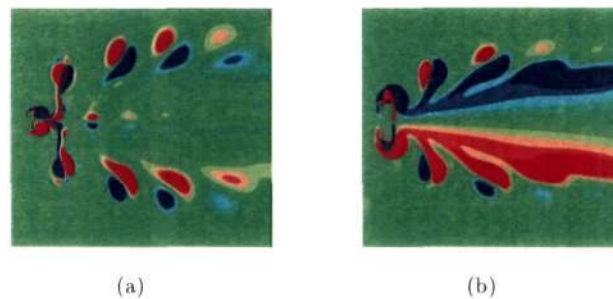


Figure 4.12: Two of the modes of shedding at $A/D = 0.175$ on a body of aspect ratio 4. (a) The S-III mode at $f_e/f_o = 2.15$. Three pairs of binary vortices are shed. (b) The S-II mode at $f_e/f_o = 4$. In this mode two binary vortices are shed during each time period.

Reynolds number. The oscillating square cylinder together with the symmetric portion of its wake corresponds roughly to a stationary body with an effective D/h less than 1. In fact the Strouhal number of the downstream portion of this figure is the same as that of a body whose aspect ratio is 0.67. In taller geometries, the mixed mode is actually encouraged to occur by merger events of vortices of one sign, some of which are evident in figures 4.9(b) and 4.9(c). The downstream behaviour again becomes antisymmetric. With all other parameters held constant, and reducing h alone, i.e., using a taller rectangular cylinder rather than a square, we would reduce the relative size of the boundary layer and therefore the strength of the shed vortex. The pressure oscillations, which normally promote antisymmetric shedding, are correspondingly reduced, and so the symmetric pattern should persist further downstream for a given oscillation frequency. This is indeed manifested (not shown).

Returning to our discussion on the aspect ratio of 4, the wake pattern changes from a Kármán street, followed by a chaotic pattern, through S-III and then S-II, followed by S-I with increase in the frequency of oscillation. The S-III mode, shown in figure 4.12(a), is simply the S-II mode with an extra pair of vortices appearing close to the centreline. It is classified separately since it appears on the other side of chaos in the transition from antisymmetric shedding. A sample of S-II shedding on this cylinder is shown in figure 4.12(b).

The dominant frequency for $f_e/f_o = 2$ is $f_s = f_o$ (figure 4.13). This is indicative of subharmonic lock-on (Barbi *et al.* (1986); Griffin & Ramberg (1974)), while the shedding is locked on to the oscillation of the cylinder in the S-III mode.

Mechanism for S-II and S-III modes

Figure 4.14 shows the time signal of the vorticity ω at the monitor point C. In the absence of a mean flow, it is easy to visualise the alternate shedding of oppositely signed vortices when

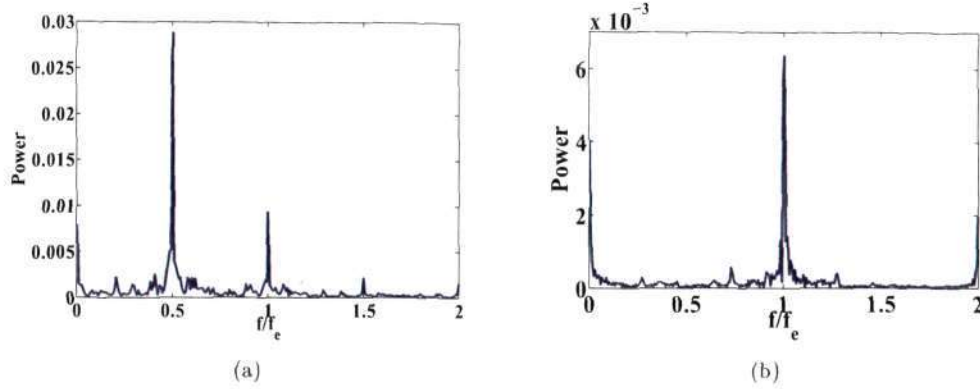


Figure 4.13: Power spectra at the monitor point A for $D/h = 4$ and $A/D = 0.175$. (a) Subharmonic shedding at $f_e/f_o = 2$. (b) The shedding is harmonic (symmetric) for $f_e/f_o = 2.15$.

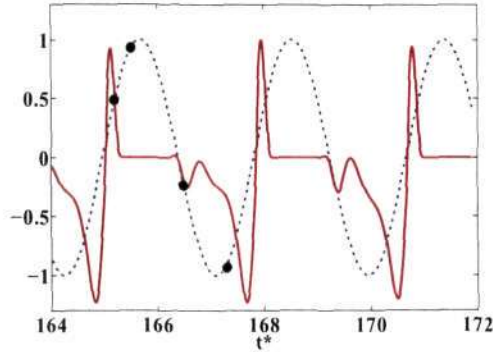


Figure 4.14: Phase information for the S-II mode for $D/h = 8$. Solid line: the vorticity ω at monitor point B . Dashed line: inlet velocity U_{total} . Here $f_e/f_o = 2$ and $A/D = 0.175$. The circles indicate the phases at which the vorticity field is shown in figures 4.15(a) - 4.15(d).

the cylinder is moving to and fro. The mean flow advects both vortices downstream. This S-II mode of shedding is aided by the ‘ground effect’. The primary vortices accelerate the fluid in the wake region towards the cylinder, and due to the larger area available on a rectangle rather than a square at the lee surface, significant vorticity of opposite sign is generated. This effect is similar to the one studied by Carnevale *et al.* (1997) on a different problem.

This ground effect is clearly visible on a rectangle of aspect ratio 8. The circles in figure 4.14 indicate the time instances at which vorticity field is plotted in figures 4.15(a) - 4.15(d). In figure 4.15(a) the cylinder is moving upstream. The primary vortices are seen to form just behind the top and bottom surfaces of the cylinder. Vorticity is continuously supplied to them in the usual manner by the boundary layers. As these primary vortices grow they accelerate the fluid in the wake region leading to the formation of boundary layers, figure 4.15(b), on the lee side of the cylinder, of oppositely-signed vorticity with respect to the primary vortices. Now, when the cylinder moves downstream there is a local reverse flow near the cylinder. This causes shape changes in both vortices. The secondary vortices continue to grow and cut off supply to the primary vortices as can be seen in Figs. 4.15(c) and 4.15(d). This cycle repeats. In the experiments of Xu *et al.* (2006) there was considerable overall reverse flow which aided the formation of opposite signed vortices on the surface of a circular cylinder. Here, aided by the ground effect, we obtain the S-II mode even without reverse flow at the inlet.

The formation of the S-III mode involves the ground effect too. However, the vorticity field

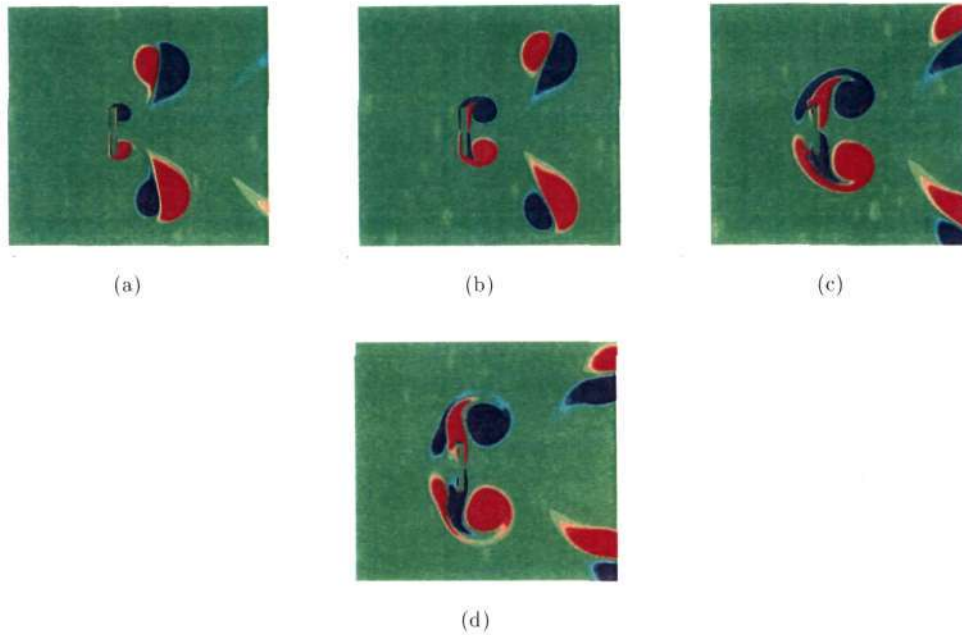


Figure 4.15: The S-II mode of vortex shedding; $D/h = 8$, $f_e/f_o = 2$ & $A/D = 0.175$. Time has been non-dimensionalized using the convective time-scale, D/U_∞ . (a) Attached primary vortices are growing. (b) Vorticity is generated on the lee side. (c) Close to the cylinder the flow is from right to left. The primary vortices are pushed apart and the secondary vortices are ‘stretched’. (d) The secondary vortices cut off the supply to primary.

is more complex than in the S-II mode during the intermediate stages. Since the frequency is slightly lower in this case, there is time for the secondary vortex to get stretched, due to the action of both the vortex being generated on the surface and the vortex which has just been dislodged from the cylinder. This leads to the pinching off of the secondary vortex at a point close to the primary vortex, and thus the generation of an extra pair of vortices which move along the centerline. Figures 4.16(a) and 4.16(b) show two phases of this process.

An obvious difference between our geometries and a circular cylinder, even when the cylinders are fixed, is that the separation points are fixed at the sharp corners in our case, but are Reynolds number dependent in the circular cylinder. No other qualitative difference is evident in this range of Reynolds numbers. The basic difference between a square and rectangular geometry is that the ground effect is more pronounced in the latter, when the two are oscillating. The larger surface available on the rear side relative to the horizontal surfaces on a rectangular cross-section means that boundary layer effects from the rear can compete with those from the top and bottom. Other things held fixed, a rectangular geometry can thus provide a range of possibilities not all accessible to a square.

Mode competition and chaos

Perdikaris *et al.* (2009) reported chaotic flow in the wake of a circular cylinder placed in a uniform flow at one particular amplitude of in-line oscillation. In their simulations the cylinder was forced at the corresponding Strouhal frequency of the fixed cylinder. At about the same time, without being aware of that work, we had obtained chaotic flow using square and rectangular cylinders. We thus confirm their appealing finding. Further, while they surmised that a competition between antisymmetric and symmetric shedding was causing chaos, they did not have direct evidence for this. In particular, their lift coefficients and spectra indicate antisymmetric shedding

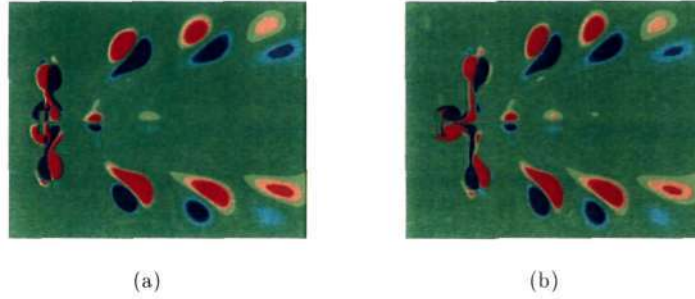


Figure 4.16: The S-III mode of vortex shedding; $D/h = 4$, $f_e/f_o = 2.15$ & $A/D = 0.175$. In both figures the cylinder is moving towards the left (upstream). (a) The stretching of secondary vortices has begun, and they are about to be dislodged from the cylinder by the next pair of primary vortices. (b) The central part of the secondary vortices have thinned, creating a pinch off of an extra pair vortices which then move along the centreline.

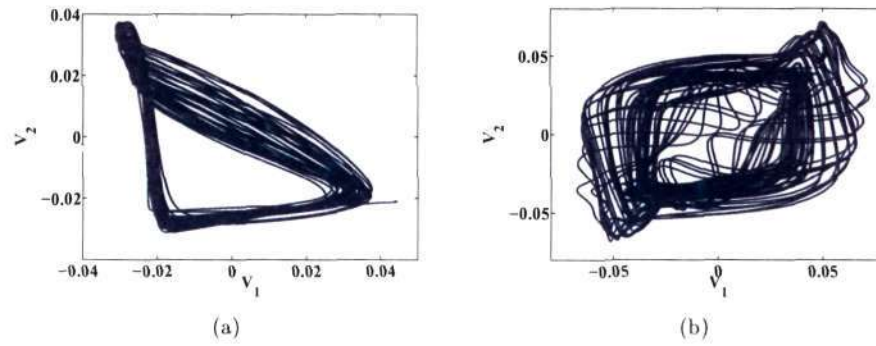


Figure 4.17: Delay plots for $D/h = 4$, $f_e/f_o = 2$ and 2.085 . The oscillation amplitude $A/D = 0.175$. The monitor point is behind the cylinder at $(0.5D, 0.35D)$. The delay plot (a) consists of closed curves, indicating periodicity, whereas (b) is characteristic of an aperiodic time signal.

under all non-chaotic conditions, so they do not have mode competition between antisymmetric and symmetric modes. For the values of nondimensional numbers used the use of a rectangular cross-section makes it easy to obtain symmetric shedding, so we are able to demonstrate that the shedding is antisymmetric at f_e less than for the chaotic flow, and symmetric for f_e greater than this value, which is a direct demonstration of mode competition in the sense of Ciliberto & Gollub (1984, 1985).

In figure 4.18(c), typical delay plots, for u_y at $f_e/f_o = 2$ and 2.085 are shown. The axes on the delay plots represent $V_1 = u_y(t + \tau)$ and $V_2 = u_y(t - \tau)$ at a suitably chosen location and delay time τ . In figure 4.17(a) the paths in phase space are closed, which indicates periodicity. The noise in the computations gives rise to a patch rather than a single path, as often happens in these computations. In spite of this noise, this figure may easily be contrasted with figure 4.17(b), which is indicative of a chaotic flow. The chaotic window is easily visualised in figure 4.18, with the antisymmetric mode, locked on to $0.5f_e$, and the S-III mode, locked on to f_e , on either side of the narrow window of chaotic flow in between.

Thus far we have obtained qualitative indications of the chaotic window. To confirm that

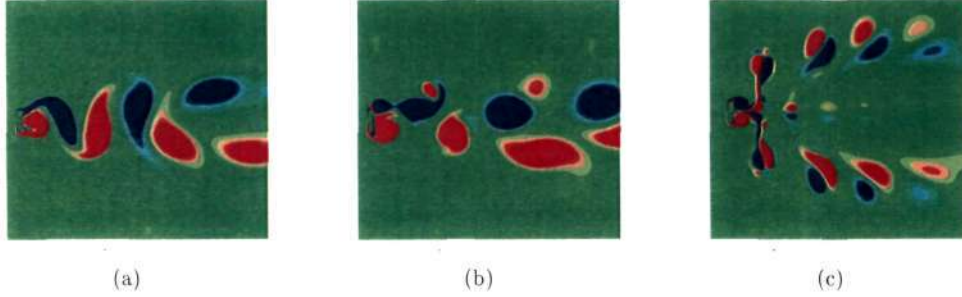


Figure 4.18: Chaotic window for $D/h = 4$. (a) $f_e/f_o = 2$, the shedding here is antisymmetric. (b) $f_e/f_o = 2.085$, the shedding is chaotic. (c) $f_e/f_o = 2.15$, S-III mode of symmetric shedding.

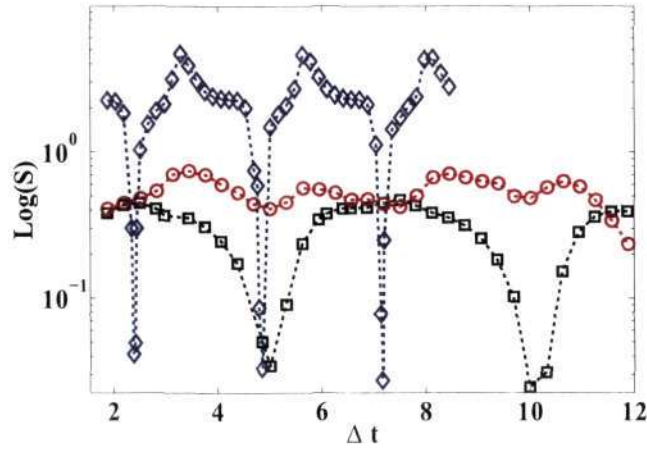


Figure 4.19: $D/h = 4$. Variation of S with Δt for different cases. Squares: $f_e/f_o = 2$, circles: $f_e/f_o = 2.085$ and diamonds: $f_e/f_o = 2.15$. The first and third curves exhibit periodicity and have sharp dips at $\Delta t = nT$ for any integer n , whereas the second curve is aperiodic.

the flow is indeed chaotic, we use a global measure $S(\Delta t)$, defined as:

$$S = \sum_i \sum_j [\omega(x_i, y_j, t_o + \Delta t) - \omega(x_i, y_j, t_o)]^2 \Delta x \Delta y. \quad (4.1)$$

Being an integrated quantity over the entire domain, S is a reliable measure of chaos. For a periodic system of period T , $S(T) = 0$. Moreover for any Δt we should have $S(\Delta t + T) = S(\Delta t)$. For $f_e/f_o = 2$ and $f_e/f_o = 2.15$, both these properties are seen in figure 4.19. In particular, a sharp dip in S for $\Delta t = nT$ for any integer n is visible. On the other hand, for $f_e/f_o = 2.085$, S remains at a high value, characterising a chaotic system.

A different behaviour is seen at $D/h = 8$. The vortex shedding mode changes from S-II to the mixed mode with S-I shedding when f_e/f_o is varied from 2 to 3.5. Figure 4.22 shows that the flow for $f_e/f_o = 2$ is periodic. However, the flow is chaotic for $f_e/f_o = 2.5$, as evidenced by the spectrum in figure 4.20. Also the arrangement of vortices at a given time is in no particular pattern, as seen in figure 4.21. The contrast in terms of the S is demonstrated in figure 4.22. A smaller region is chosen to improve the contrast. The variation of S for $f_e/f_o = 2$ is seen to be periodic, whereas for $f_e/f_o = 2.5$ it is not.

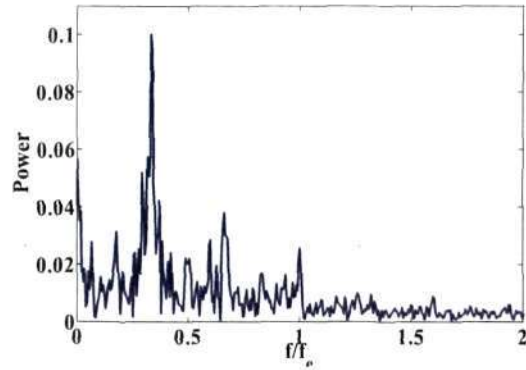


Figure 4.20: $D/h = 8$, $f_e/f_o = 2.5$ & $A/D = 0.175$. The spectrum of the time signal of u_y is broadband.

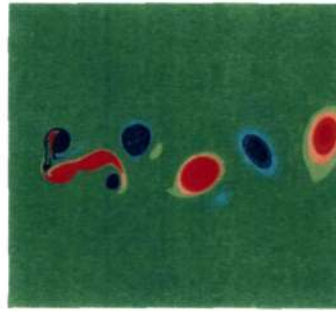


Figure 4.21: $D/h = 8$, $f_e/f_o = 2.5$ & $A/D = 0.175$. The arrangement of vortices is unordered, showing that the flow is chaotic.

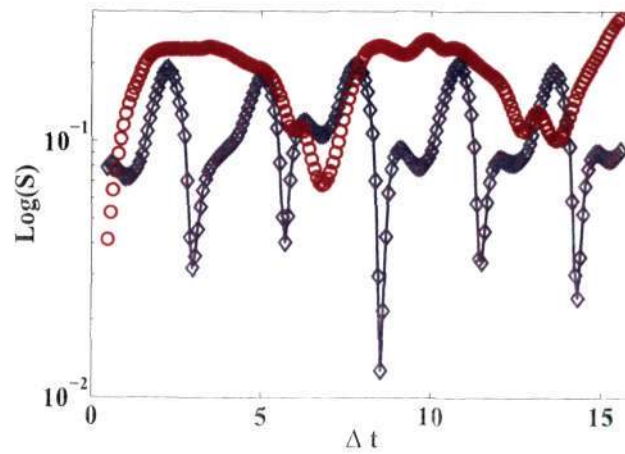
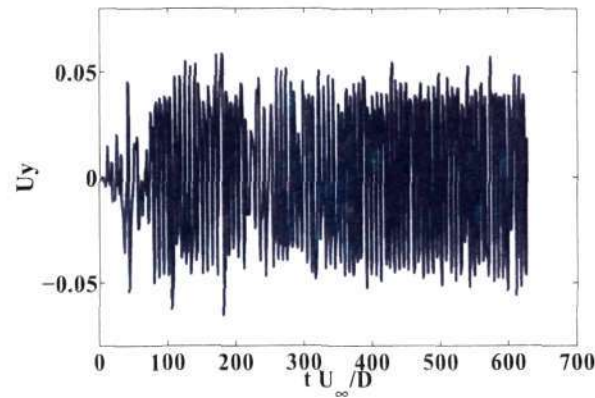


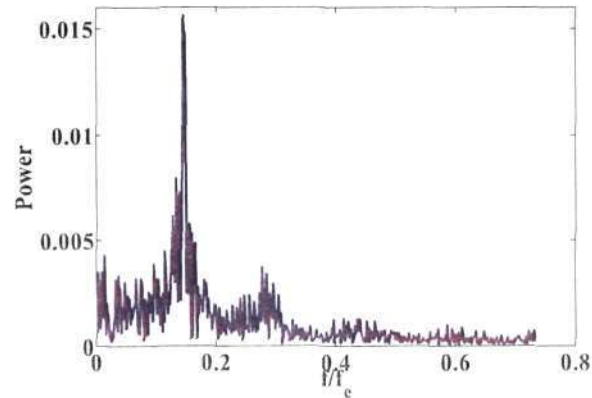
Figure 4.22: $D/h = 8$. Variation of S with Δt in a region $x/D = 2.5 - 8.75$. Diamonds: $f_e/f_o = 2$, and is repetitive indicating periodicity. Circles: $f_e/f_o = 2.5$, and shows the aperiodic nature of the vorticity field in that region.

Chaos in flow past an inline oscillating square cylinder (?)

In contrast to the results discussed above, for a rectangular geometry a square geometry seems to be different. In the latter mode competition does not play a role in the chaotic flow obtained in the case of a square cylinder oscillating at the Strouhal frequency. The nondimensional numbers used in this case were: $Re = 200$, $f_e/f_o = 1$ and $0.1 \leq A/D \leq 1$. Chaotic flow is observed at $A/D = 1$, and the route seems to be the Ruelle-Takens route to chaos. In this route incommensurate frequencies are generated in the system with the increase in the governing nondimensional parameter. A strange attractor appears after the generation of three incommensurate frequencies, which suddenly leads to chaos. The generation of incommensurate frequencies was observed as A/D was varied from 0.1 to 1. However, the data is not conclusive enough to support this. This does indicate that there might be different routes to chaos depending on the range of nondimensional numbers being used to study the flow. Perdikaris *et al.* (2009) too observed chaos at this forcing frequency, and our results qualitatively indicate that it was not mode competition, as claimed by them, which led to chaotic flow. Figures 4.23(a) and 4.23(b) show the time signal and spectrum for the chaotic flow in square cylinder case.



(a)



(b)

Figure 4.23: Time signal of u_y at the monitor point A for square cylinder. $Re = 200$, $f_e/f_o = 1$ and $A/D = 1$. (a) The time signal indicates the chaotic nature of flow, and (b) the broadband spectrum confirms this.

Chapter 5

Vortex Merger

This chapter describes a problem that is different from the main work of this thesis. It is a study being done with *Rohith Swaminathan*, and a detailed description will be presented in his thesis. Here, the code developed is described in some detail, and some preliminary results are presented.

Merger of two vortices is one the important processes that characterizes a two-dimensional turbulent flow in which a large number of vortices merge depending on their signs (clockwise or anticlockwise). A detailed study of this phenomenon is important as it would lead to a better understanding of the process which drives fluid turbulence in two dimensions. There have been several studies in the past, some of them being: Cerretelli & Williamson (2003), Brandt & Nomura (2006), Meunier *et al.* (2005), Dixit (2010), etc. In this chapter, some aspects of the Fourier spectral method and its application to the above mentioned problem are discussed. Preliminary results on the merger of two Gaussian vortices are also presented.

5.1 Governing equations and the Fourier spectral method

In the case of two-dimensional flows, it is advantageous to solve the vorticity equation as it does not involve the pressure term. This equation is derived from the Navier-Stokes equation by taking the curl of the latter. The equation is

$$\frac{\partial \omega}{\partial t} + u \frac{\partial \omega}{\partial x} + v \frac{\partial \omega}{\partial y} = \nu \left(\frac{\partial^2 \omega}{\partial x^2} + \frac{\partial^2 \omega}{\partial y^2} \right). \quad (5.1)$$

Here, ω is the vorticity field, u and v are the x and y components of the velocity and ν is the kinematic viscosity of the fluid. The velocity components are expressed in terms of the stream function, ψ , which are given by

$$u = \frac{\partial \psi}{\partial y}; \quad v = -\frac{\partial \psi}{\partial x}. \quad (5.2)$$

The stream function can be calculated from the vorticity field by solving the Poisson equation

$$\nabla^2 \psi = -\omega. \quad (5.3)$$

In the Fourier spectral method, eqns. 5.1 and 5.3 are solved in Fourier space with periodic boundary conditions. This numerical approach is the two-dimensional counterpart of the “box turbulence” in three dimensions, where the turbulent flow is considered to be both homogeneous and isotropic. The Fourier transform of the vorticity field is given by

$$\hat{\omega}_{\mathbf{k}}(t) = \int_0^{2\pi} \omega(x, y, t) e^{-i\mathbf{k} \cdot \mathbf{r}} dx dy, \quad (5.4)$$

where \mathbf{k} and \mathbf{r} are the wavenumber and displacement vectors and $\hat{\omega}_{\mathbf{k}}(t)$ is the vorticity in Fourier space. The domain size is taken to be 2π , and hence the choice of the limits of integration. The flow parameters have no spatial dependence in Fourier space as they have been integrated over space.

Now, taking the transform of eqns. 5.1 and 5.3 one obtains

$$\frac{d\widehat{\omega}_k}{dt} + u \frac{\partial \widehat{\omega}}{\partial x} + v \frac{\partial \widehat{\omega}}{\partial y} = -\nu k^2 \widehat{\omega}_k, \quad (5.5)$$

and,

$$\widehat{\psi}_k = \frac{\widehat{\omega}_k}{k^2}, \quad (5.6)$$

where $k^2 = k_x^2 + k_y^2$. Equation 5.5 is an ordinary differential equation in $\widehat{\omega}_k$ and any of the standard explicit time-marching schemes (first order Euler, Runge-Kutta, Adams-Bashforth, etc) can be used to solve the above equations for a given initial condition. However, the most difficult part of the eqn. 5.5 are the convolution sums, $u \frac{\partial \widehat{\omega}}{\partial x}$ and $v \frac{\partial \widehat{\omega}}{\partial y}$, which represent the interaction between different wavenumbers. If there are N wavenumbers, then it would require $O(N^2)$ operations to compute each convolution sum in Fourier space. This operation is a very expensive one, and to circumvent this difficulty the convolution sums are evaluated in real space (Canuto *et al.* (2006)). This method is widely known as the pseudo-spectral method. For the second term in eqn. 5.5, first the terms \widehat{u} and $-ik_x \widehat{\omega}$ are calculated, then they are inverse transformed to give u and $\frac{\partial \omega}{\partial x}$ in real space which are multiplied giving $u \frac{\partial \omega}{\partial x}$, and finally the Fourier transform of this term gives the required convolution sum. The third term in eqn. 5.5 is obtained similarly.

However, one has to take care of the corruption of data coming in from higher wave numbers. This effect is called the aliasing effect. This can be understood as follows: let the size of the domain be 2π and let there be N grid points. The j^{th} co-ordinate is then given by $x_j = 2\pi j/N$. Let $f(x)$ and $g(x)$ be two functions of x , and $F(k)$ and $G(k)$ be their discrete Fourier transforms, i.e.,

$$F(k) = \sum_{j=0}^{N-1} f(x_j) e^{-\frac{2\pi i j k}{N}}; \quad G(k) = \sum_{j=0}^{N-1} g(x_j) e^{-\frac{2\pi i j k}{N}}. \quad (5.7)$$

Functions of one variable are considered for simplicity. The product of the functions is given by:

$$s = f(x)g(x); \quad (5.8)$$

and its convolution is:

$$C = \sum_{k=-N/2}^{N/2-1} s(x_j) e^{-\frac{2\pi i j k}{N}}. \quad (5.9)$$

Substituting eqn. 5.8 and the inverse transforms in 5.9, we get:

$$C = \sum_{k=-N/2}^{N/2-1} f(x_j)g(x_j) e^{-\frac{2\pi i j k}{N}}, \quad (5.10)$$

where $i = \sqrt{-1}$. Substituting the discrete transforms of f and g in eqn. 5.10 we have

$$C = \sum_k \left(\sum_p F_p e^{\frac{2\pi i j p}{N}} \sum_q G_q e^{\frac{2\pi i j q}{N}} \right) e^{-\frac{2\pi i j k}{N}}. \quad (5.11)$$

Here, p and q are wavenumbers too. The summation is from $-N/2$ to $N/2 - 1$ and will be omitted in the subsequent expressions. Simplifying this gives,

$$C = \sum_p \sum_q F_p G_q \sum_k e^{\frac{2\pi i j (\rho+q-k)}{N}}. \quad (5.12)$$

This can be written as

$$C = \sum_{p+q=k} F_p G_q + \sum_{p+q=k \pm N} F_p G_q. \quad (5.13)$$

The first term on the right hand side of eqn. 5.13 is the required convolution sum and the second term is the aliasing error. It is easily seen that when $p + q \neq k$ the second term too contributes to the convolution sum, which as mentioned earlier is the interference of higher wave numbers.

De-aliasing is carried out by padding the signals with zeroes at the ends in the second stage of the pseudo-spectral method, i.e. the inverse Fourier-transformed signals are padded. The two signals are then multiplied in real space and product is Fourier transformed. The relevant data is extracted from this transform. This method of padding makes the amplitudes of higher wave number terms zero, thus making their contribution zero. This process is shown below:

$$F(k), G(k) \xrightarrow{\text{Inversetransform}} f(x), g(x) \xrightarrow{\text{Padding}} f_1(x), g_1(x) \xrightarrow{\text{MultiplyandFouriertransformtheproduct}} f_1(x)g_1(x) \xrightarrow{\text{Extract}} f(x)g(x).$$

The minimum size of the padded signal is $3N/2$ for a given signal of size N . These methods are discussed in detail in the books of Canuto *et al.* (2006) and Boyd (2000).

5.2 Merger of same signed Gaussian vortices

The Fourier spectral code developed is used to study the merger of two, three and four Gaussian vortices in a homogeneous fluid. Periodic boundary conditions are used in both x and y directions. The domain size used is $2\pi \times 2\pi$ with different grid points depending on Re . Here, Γ is the circulation of one vortex, a_o is the initial diameter and b_o is some measure of the distance between vortices based on their alignment. Re is defined as: $Re = \Gamma/\nu$ and the convective time scale is $t_c = 2\pi a_o^2/\Gamma$.

Some of the plots shown in this section were first used in my BE thesis, but have been reproduced here with more analyses which were done recently.

5.2.1 Merger of two vortices: code validation

The results of validation for the case of merger of two vortices is discussed here. The results obtained from the code were compared with that of Brandt & Nomura (2006), and Dixit (2010).

In fig. 5.1, the evolution of the distance between the vortices is compared with that obtained by Brandt & Nomura (Brandt & Nomura (2006)). The distance is non-dimensionalized with the initial distance, and the time with the convective time scale. The data presented in their article is only upto $t^* \approx 0.92$, and the complete merger process is shown in the result obtained by us. As evident, the results are in excellent agreement. One interesting point to note is that they used a finite difference scheme to solve the governing equations with 2048^2 grid points, but in our computation done with spectral method the same accuracy is obtained by using just 256^2 grid points. Similar comparison was done for $Re = 2000$ with Dixit (2010), and an excellent agreement was found. This is shown in fig. 5.2.

The events leading to the merger of two vortices is shown in fig. 5.3. The vortices, in the initial stage, grow due to viscous diffusion.

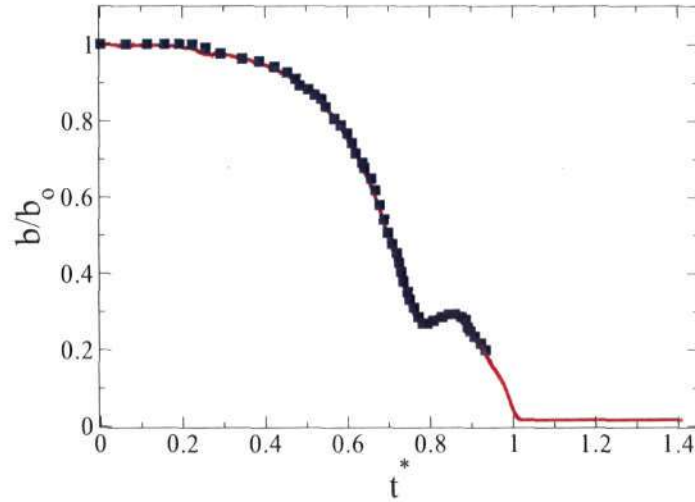


Figure 5.1: The plot shows the comparison of the evolution of distance between the two vortices with time for $Re = 1000$. Squares: Brandt & Nomura (2006); Red curve: present study. Here, time is non-dimensionalized with the convective time scale: $t^* = t2\pi^2b_0^2/\Gamma$.

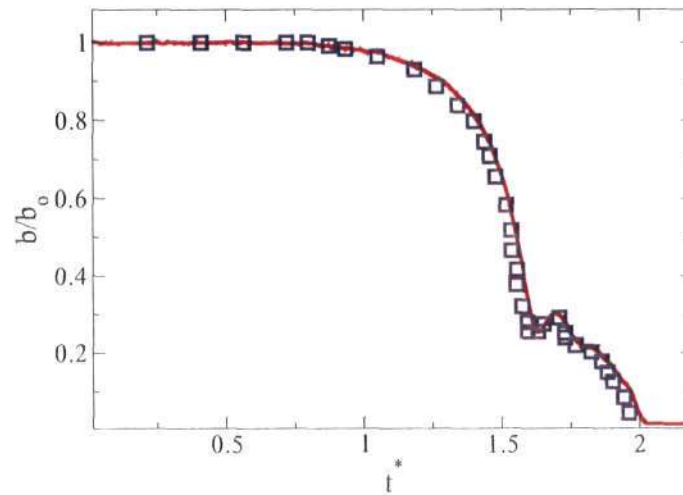


Figure 5.2: The plot shows the comparison of the evolution of distance between the two vortices with time for $Re = 2000$. Squares: Dixit (2010); Red curve: present study. Here, time is non-dimensionalized with the convective time scale: $t^* = t2\pi^2b_0^2/\Gamma$.

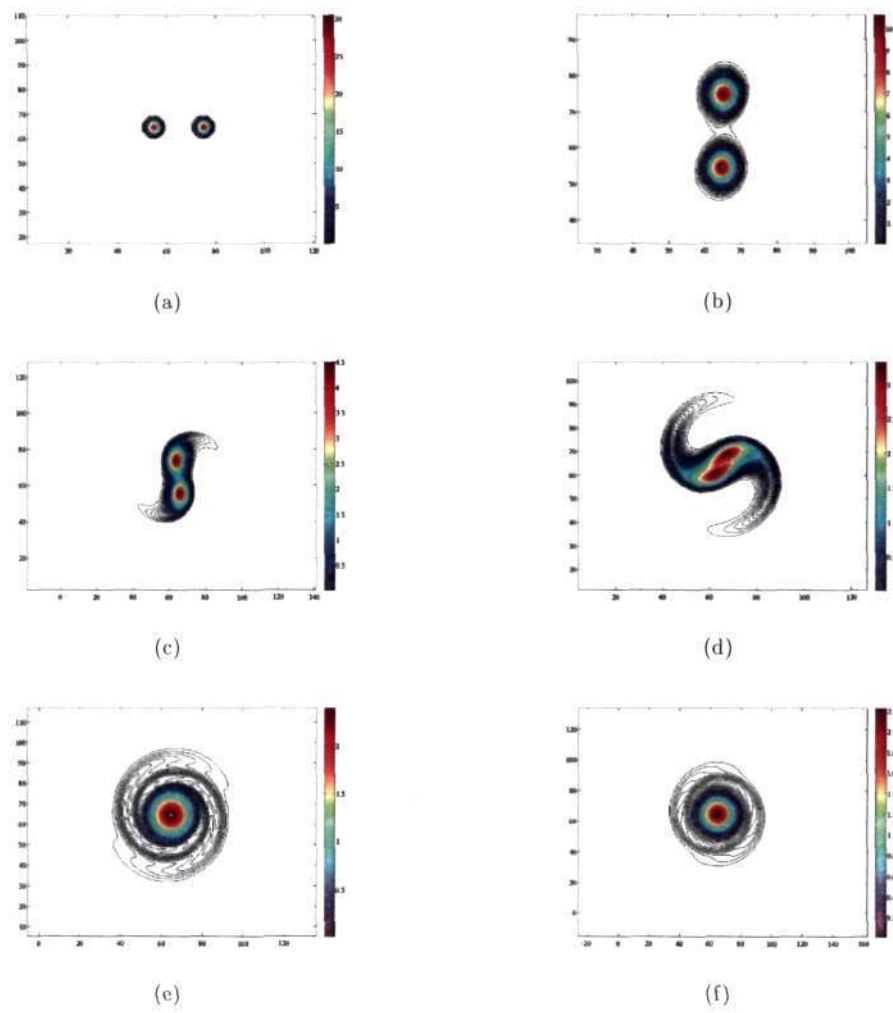


Figure 5.3: Evolution of two vortices in an unstratified fluid for $Re = 1000$.

Chapter 6

Conclusions

In this thesis, vortex shedding from both fixed and inline oscillating rectangular cylinders has been studied numerically. The Lattice-Boltzmann equation (LBE) was used to solve for the flow. Rectangular cylinders of aspect ratios (D/h) 1 – 8 were used in this study, and this is the first such study to our knowledge. Grid stretching was employed to reduce the computation time. The code was validated for both fixed and oscillating cases with standard results available in the literature.

In the case of fixed rectangular cylinders the following were studied: the variation of bubble size for $Re < Re_{cr}$, calculation of Re_{cr} based on decay and growth rates of disturbances in the wake, the variation of St with Re for some geometries ($D/h = 1, 2 \& 4$) and b/a ratios for the Kármán streets at the same Re . It is found that the flow is steady even when $L/D > 3$ for all geometries considered, and upto $L/D = 4$ for $D/h = 8$. It was shown that for Re close to Re_{cr} the growth rates vary linearly with $Re - Re_{cr}$ as predicted by the linear theory. Re_{cr} was found to decrease slightly with increasing D/h , confirming our intuition.

In the case of inline oscillating rectangular cylinders, all the symmetric modes reported in the literature were reproduced. To our knowledge, this is the first numerical study to report the $S - II$ mode of symmetric shedding, first discovered by Xu *et al.* (2006) in their experiments. A new symmetric mode, named $S - III$, was discovered and the mechanism of its formation was discussed. It was also shown that the flow becomes chaotic for certain values of forcing parameters, and windows of chaos, qualitatively similar to the ones discovered by Ciliberto & Gollub (1984), exist in the case of flow past an inline oscillating cylinder too. A global parameter was constructed to 'quantify' chaos and the spatio-temporal aperiodicity of the chaotic flow was demonstrated.

Also, a previously developed Fourier-Spectral code was validated with existing results in the literature, and sample results discussed.

References

- ANSUMALI, S., CHIKATAMARLA, S. S., FROUZAKIS, C. E. & BOULOUCHOS, K. 2003 Entropic lattice boltzmann simulation of the flow past square cylinder. *Int. J. Modern Phys. C* .
- BARBI, C., FAVIER, D. P., MARESCA, C. A. & TELIONIS, D. P. 1986 Vortex shedding and lock-on of a circular cylinder in oscillatory flow. *J. Fluid Mech.* **170**, 527–544.
- BOYD, J. P. 2000 *Chebyshev and Fourier Spectral Methods*. New York: Dover.
- BRANDT, L. K. & NOMURA, K. K. 2006 The physics of vortex merger and the effects of ambient stable stratification. *J. Fluid Mech.* **592**, 413–446.
- CANUTO, C., HUSSAINI, M. Y., QUARTERONI, A. & ZANG, T. A. 2006 *Spectral Methods Fundamentals in Single Domains*. Heidelberg: Springer.
- CARNEVALE, G. F., FUENTES, O. U. V. & ORLANDI, P. 1997 Inviscid dipole-vortex rebound from a wall or coast. *J. Fluid Mech.* **351**, 75–103.
- CERRETELLI, C. & WILLIAMSON, C. H. K. 2003 The physical mechanism for vortex merging. *J. Fluid Mech.* **475**, 41–77.
- CHEN, S. & DOOLEN, G. D. 1998 Lattice boltzmann method for fluid flows. *Ann. Rev. Fluid Mech.* **30**, 329–364.
- CILIBERTO, S. & GOLLUB, J. P. 1984 Pattern competition leads to chaos. *Phys. Rev. Letters* **52**, 922–926.
- CILIBERTO, S. & GOLLUB, J. P. 1985 Chaotic mode competition in parametrically forced surface waves. *J. Fluid Mech.* **158**, 381–398.
- DIXIT, H. N. 2010 Some studies on vortices with density stratification. PhD thesis, Jawaharlal Nehru Centre for Advanced Scientific Research, Bangalore, India.
- GRIFFIN, O. N. & RAMBERG, S. E. 1974 The vortex street wakes of vibrating cylinders. *J. Fluid Mech.* **66**, 553–576.
- H. OERTEL, J. 1990 Wakes behind blunt bodies. *Ann. Rev. Fluid Mech.* **22**, 539–562.
- HARRIS, S. 2004 *An Introduction to the theory of the Boltzmann equation*. New York: Dover.
- HE, X. & LUO, L. 1997 Theory of the lattice boltzmann method: From the boltzmann equation to the lattice boltzmann equation. *Phys. Rev. E* **56**, 6811–6817.

- HE, X., LUO, L. & DEMBO, M. 1996 Some progress in lattice boltzmann method. part i. nonuniform mesh grids. *J. Comp. Physics* **129**, 357–363.
- KONSTANTINIDIS, E. & BALABANI, S. 2007 Symmetric vortex shedding in the near wake of a circular cylinder due to streamwise perturbations. *J. Fluids Struct.* **23**, 1047–1063.
- LANDAU, L. D. & LIFSHITZ, E. M. 1981 *Physical Kinetics*. Pergamon Press Ltd.
- LANDAU, L. D. & LIFSHITZ, E. M. 2005a *Fluid Mechanics*. New Delhi: Butterworth-Heinemann.
- LANDAU, L. D. & LIFSHITZ, E. M. 2005b *Statistical Physics Part 1*. New Delhi: Butterworth-Heinemann.
- MEUNIER, P., DIZES, S. L. & LEWEKE, T. 2005 Physics of vortex merging. *Comptes Rendus Physique* **6** 4-5, 431–450.
- MINESWITSCH, S., FRANKE, R. & RODI, W. 1994 Numerical investigation of laminar vortex-shedding flow past a square cylinder oscillating in line with the mean flow. *J. Fluids Struct.* **8**, 787–802.
- OKAJIMA, A. 1982 Strouhal numbers of rectangular cylinders. *J. Fluid Mech.* **123**, 379–398.
- OKAJIMA, A., YI, D., SAKUDA, A. & NAKANO, T. 1997 Numerical study of blockage effects on aerodynamic characteristics of an oscillating rectangular cylinder. *J. Wind Eng. Ind. Aerodyn.* **67-68**, 91–102.
- ONGOREN, A. & ROCKWELL, D. 1988 Flow structure from an oscillating cylinder part - 2. mode competition in the near wake. *J. Fluid Mech.* **191**, 225–245.
- PERDIKARIS, P. G., KAIKTSIS, L. & TRIANTAFYLLOU, G. S. 2009 Chaos in a cylinder wake due to forcing at the strouhal frequency. *Phys. Fluids* **21**, 101705.
- PROVANSAL, M., MATHIS, C. & BOYER, L. 1989 Benard-von karman instability: transient and forced regimes. *J. Fluid Mech.* **182**, 1–22.
- SHARMA, A. & ESWARAN, V. 2004 Heat and fluid flow across a square cylinder in the two-dimensional laminar flow regime. *Num. Heat Transfer Part A*, **45**, 247–269.
- SREENIVASAN, K. R., STRYKOWSKI, P. J. & OLINGER, D. J. 1987 Hopf bifurcation, landau equation and vortex shedding behind circular cylinders. *Forum on unsteady flow separation, Cincinnati, Ohio, June 14-17, 1-13 (1987), Proceedings (A88-14141 03-34)*. New York, American Society of Mechanical Engineers pp. 1–13.
- SUCCI, S. 2006 *The Lattice Boltzmann Equation for Fluid Dynamics and Beyond*. Norfolk: Oxford University Press.
- VITTORI, G. & BLONDEAUX, P. 1993 Quasiperiodicity and phase locking route to chaos in 2-d oscillatory flow around a circular cylinder. *Phys. Fluids A* **5(8)**, 1866–1868.

- WILLIAMSON, C. H. K. 2000 Vortex dynamics in the cylinder wake. *Annu. Rev. Fluid Mech.* **28**, 477-539.
- WOLF-GLADROW, D. A. 2000 *Lattice-Gas Cellular Automata and Lattice Boltzmann Methods*. Heidelberg: Springer.
- XU, S. J., ZHOU, Y. & WANG, M. H. 2006 A symmetric binary-vortex street behind a longitudinally oscillating cylinder. *J. Fluid Mech.* **556**, 27-43.

621.437

P11

